

## Raman mapping of photodissociation regions in Orion

WILLIAM J. HENNEY<sup>1</sup>

<sup>1</sup>*Instituto de Radioastronomía y Astrofísica, Universidad Nacional Autónoma de México, Apartado Postal 3-72, 58090 Morelia, Michoacán, Mexico*

### Abstract

I show that the broad Raman-scattered wings of H $\alpha$  can be used to map neutral gas illuminated by high-mass stars in star forming regions. The near wings ( $\Delta\lambda \approx \pm 10$  Å) trace neutral hydrogen columns of about  $5 \times 10^{20}$  cm $^{-2}$ , while the farther wings ( $|\Delta\lambda| > 30$  Å) trace columns of about  $5 \times 10^{21}$  cm $^{-2}$ . Absorption features in the pseudo-continuum at 6633 and 6664 Å correspond to neutral oxygen far-ultraviolet absorption lines at 1027.43 Å and 1028.16 Å.

**Keywords:** Atomic physics; Radiative transfer; Photodissociation regions

### 1. INTRODUCTION

Raman scattering is the inelastic analog of Rayleigh scattering by atoms or molecules. Both processes begin with a radiation-induced transition of an electron to a virtual bound state (non-eigenstate). In Rayleigh scattering, the electron returns to its original state, resulting in the radiation being re-emitted with its original frequency (elastic scattering). In Raman scattering, on the other hand, the electron undergoes a transition to a different excited state, resulting in radiation being re-emitted at a much lower frequency. See Figure 1 for an illustration of the process. Recently, Dopita et al. (2016) identified exceedingly broad wings to the H $\alpha$  6563 Å line in the Orion Nebula and a number of H II regions in the Magellanic Clouds, which they ascribe to Raman scattering of ultraviolet radiation in the vicinity of the Ly $\beta$  1025 Å transition. Raman scattering in astrophysical sources was first identified in symbiotic stars (Schmid 1989), where FUV O VI emission lines at 1032 and 1038 Å produce broad emission features at 6827 and 7088 Å. This illustrates a curious feature of Raman scattering (Nussbaumer et al. 1989): the relative width  $\Delta\lambda/\lambda$  of spectral features is amplified by a factor  $\lambda(\text{H}\alpha)/\lambda(\text{Ly}\beta) \approx 6.4$  when passing from the FUV to the optical domain.

Dopita et al. (2016) propose that the Raman wings form at the transition zone near the ionization fronts in H II regions. However, the total neutral hydrogen column through the ionization front can be no more than about  $10/\sigma_0 \approx 2 \times 10^{18}$  cm $^{-2}$ , where  $\sigma_0 \approx 6.3 \times 10^{-18}$  cm $^2$  is the ground-state hydrogen photoionization cross section at threshold (Osterbrock & Ferland 2006). The Raman scattering cross section at wavelengths responsible for the observed wings is much lower than this:  $\sigma_{\text{Raman}} \sim 10^{-21}$  cm $^2$  (Chang et al. 2015), meaning that the Raman scattering optical depth through the ionization front is only of order 0.001. A vastly larger column density of neutral hydrogen ( $\approx 10^{21}$  cm $^{-2}$ ) is available in the photodissociation region (PDR) outside the ionization front, so it is more likely that Raman scattering will occur there instead, so long as there is sufficient far ultraviolet radiative flux.

This paper is organized as follows. § 2 recapitulates the basic theory of Raman scattering, concentrating on the wavelength transformation from the FUV domain around Ly $\beta$  to optical domain around H $\alpha$ . In addition, polynomial fits are provided to the wavelength dependence of the total (Rayleigh plus Raman) scattering cross section and the Raman H $\alpha$  branching ratio. § 3 then presents archival VLT-MUSE integral field spectroscopy of the Orion Nebula, which allows the broad H $\alpha$  wings to be spatially mapped in unprecedented detail and compared with other tracers of ionized and neutral zones in the nebula. Two components of the O I UV resonance multiplet  $2p^4\ ^3P \rightarrow 3d\ ^3D^0$  are detected as absorption features at 6633 and 6664 Å against the H $\alpha$  Raman wings. § 4 presents archival Keck-HIRES slit spectroscopy, which shows the profile of the 6664 Å absorption line with an effective velocity resolution of 1 km s $^{-1}$ . § 5 discusses the implications of these results for the structure and dynamics of the PDRs in Orion, together with the prospects for using Raman spectral mapping as a diagnostic tool in the study of other high-mass star formation regions.

### 2. RAMAN SCATTERING THEORY

When a photon is Raman-scattered from the vicinity of Ly $\beta$  (UV domain) to the vicinity of H $\alpha$  (optical domain) its wavelength is transformed from  $\lambda_1$  to  $\lambda_2$ . Intervals in frequency ( $\nu = c/\lambda$ ) or wavenumber ( $\tilde{\nu} = 1/\lambda$ ) space are conserved between the two

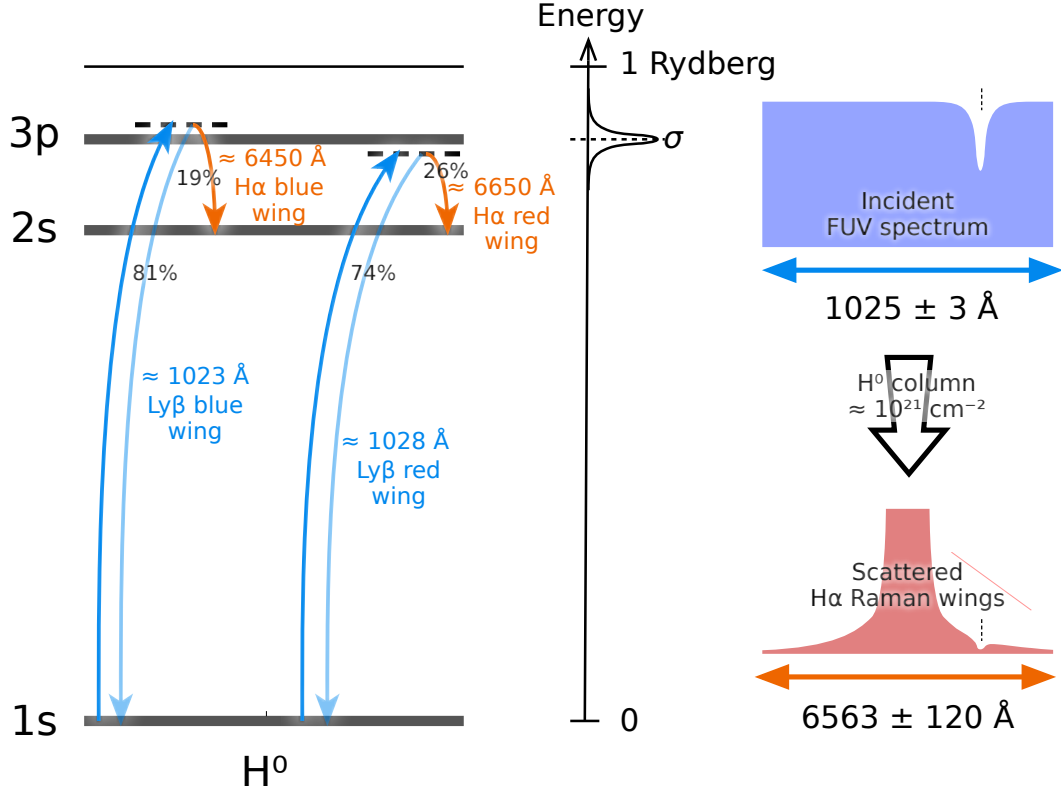


**Figure 1.** Schematic illustration of Raman scattering of photons from the Ly $\beta$  wings to the H $\alpha$  wings. The relevant energy levels of neutral hydrogen are shown at left. Far ultraviolet photons that are shifted by about  $\Delta\lambda_1 = \pm 1$  to 3 Å from the Ly $\beta$  rest wavelength can excite transitions from the ground 1s level to a virtual state adjacent to 3p. Most such excitations decay back to 1s (Rayleigh scattering), but in about one-fifth of cases the decay is to 2s instead (Raman scattering). The scattering cross section falls approximately as  $\Delta\lambda_1^{-2}$ , which gives broad Lorentzian wings to the H $\alpha$  line, as shown at right. A bandwidth of  $\Delta\lambda_1 = \pm 3$  Å around Ly $\beta$  is transformed to a bandwidth  $\Delta\lambda_2 \approx \pm 120$  Å around H $\alpha$ . A narrow absorption line in the incident FUV spectrum (vertical thin dashed line) becomes a much broader notch in the scattered wings.

**Table 1.** FUV/optical wavelength equivalencies for Raman scattering

Ion	Transition	$J_i \rightarrow J_k$	$\lambda_1, \text{ Å}$	$\tilde{\nu}_1, \text{ cm}^{-1}$	$\Delta\tilde{\nu}, \text{ cm}^{-1}$	$\tilde{\nu}_2, \text{ cm}^{-1}$	$\lambda_2, \text{ Å}$	$\lambda_{\text{air}}, \text{ Å}$
			....	Ly $\beta$ , $n = 1$	....	.....	H $\alpha$ , $n = 2$	.....
H I	$ns^2 \text{S} \rightarrow 3p^2 \text{P}$	$\frac{1}{2} \rightarrow \frac{1}{2}, \frac{3}{2}$	1025.72220	97492.283	0.000	15233.329	6564.553	6562.740
O I	$2s^2 2p^4 \text{P} \rightarrow 2s^2 2p^3(^4\text{S}) 3d^3 \text{D}^o$	$0 \rightarrow 1$	1028.15729	97261.383	-230.900	15002.429	6665.587	6663.747
		$1 \rightarrow 1$	1027.43139	97330.100	-162.183	15071.146	6635.196	6633.364
		$1 \rightarrow 2$	1027.43077	97330.159	-162.124	15071.205	6635.170	6633.338
		$2 \rightarrow 1$	1025.76339	97488.369	-3.914	15229.415	6566.240	6564.427
		$2 \rightarrow 2$	1025.76276	97488.429	-3.854	15229.475	6566.215	6564.401
		$2 \rightarrow 3$	1025.76170	97488.530	-3.753	15229.576	6566.171	6564.358
Si II	$3s^2 3p^2 \text{P}^o \rightarrow 3s^2 5s^2 \text{S}$	$\frac{1}{2} \rightarrow \frac{1}{2}$	1020.6989	97972.086	+479.803	15713.132	6364.104	6362.345
		$\frac{1}{2} \rightarrow \frac{3}{2}$	1023.7001	97684.859	192.576	15425.905	6482.602	6480.811

domains. For example the wavenumber displacement from the H $\alpha$  line center can be written in two ways:

$$\Delta\tilde{v} = \tilde{v}_1 - \tilde{v}(\text{Ly}\beta) = \tilde{v}_2 - \tilde{v}(\text{H}\alpha), \quad (1)$$

from which it follows that

$$\lambda_2 = \left( \frac{1}{\lambda(\text{H}\alpha)} + \frac{1}{\lambda_1} - \frac{1}{\lambda(\text{Ly}\beta)} \right)^{-1}. \quad (2)$$

The wavelengths  $\lambda(\text{Ly}\beta)$  and  $\lambda(\text{H}\alpha)$ , together with their corresponding wavenumbers, are given in Table 1 (all wavelengths are on the vacuum scale unless otherwise noted). For both lines, a weighted average over the 3p  $^2\text{P}_{1/2}$  and 3p  $^2\text{P}_{3/2}$  upper levels is used, assumed to be populated according to their statistical weights, with individual component wavelengths obtained from Tab. XXVIII of Mohr et al. (2008). Note that the electric dipole selection rules mean that only 3p  $\rightarrow$  2s transitions contribute to H $\alpha$  in the Raman scattering context. The wavelength is therefore slightly shorter than the value obtained for the H $\alpha$  recombination line, which includes additional contributions from 3s  $\rightarrow$  2p and 3d  $\rightarrow$  2p. The shift is of order  $-0.05 \text{ \AA}$  or  $-2 \text{ km s}^{-1}$  with respect to the Case B results reported in Tab. 6a of Clegg et al. (1999).

Also listed in Table 1 are the Raman transformations  $\lambda_1 \rightarrow \lambda_2$  for the rest wavelengths of transitions between the ground  $2s^2 2p^4 3P$  term of neutral  $^{16}\text{O}$  and the excited  $2s^2 2p^3 3d 3D^0$  term. The O $\alpha$  data is obtained from highly accurate laser metrology (Ivanov et al. 2008; Marinov et al. 2017), with a precision of  $0.08 \text{ cm}^{-1}$  or better. The fine structure splitting between the  $J_k$  levels of the excited term ( $\sim 0.1 \text{ cm}^{-1}$ ) is much smaller than that between the  $J_i$  levels of the ground term ( $\sim 100 \text{ cm}^{-2}$ ), so that the 6 transitions fall into 3 well-separated groups. The three transitions from the lowest energy  $J_i = 2$  level are very close to Ly $\beta$  ( $\Delta\tilde{v} \approx 4 \text{ cm}^{-1}$ ), whereas the two transitions from  $J_i = 1$  ( $\Delta\tilde{v} \approx 162 \text{ cm}^{-1}$ ) and the single transition from  $J_i = 0$  ( $\Delta\tilde{v} \approx 231 \text{ cm}^{-1}$ ) lie increasingly to the red. The corresponding wavelengths in the optical domain,  $\lambda_2$ , are therefore on the red side of H $\alpha$ . The final column of the table uses STP refractive indices (Greisen et al. 2006) to convert  $\lambda_2$  to air wavelengths,  $\lambda_{\text{air}}$ , for ease of comparison with ground-based optical spectroscopy. The resultant wavelength is  $6663.747 \text{ \AA}$  for the line from  $J_i = 0$ , with an uncertainty of about  $0.004 \text{ \AA}$ , which is much smaller than typical observational precision (for instance,  $0.07 \text{ \AA}$  for a very high resolution spectrograph with resolving power of  $R = 10^5$ ). The two lines from  $J_i = 1$ , with a separation of  $0.028 \text{ \AA}$ , will always be blended in observations, giving a mean wavelength of  $6633.347 \text{ \AA}$  (assuming the upper levels are distributed according to statistical weight  $2J_k + 1$ ). Similarly, the three lines from  $J_i = 2$  have a mean wavelength of  $6564.386 \text{ \AA}$ , but this is so close to H $\alpha$  (corresponding to a Doppler shift of  $+75 \text{ km s}^{-1}$ ) that it would be very difficult to observe.

The final section of Table 1 gives data for a resonance doublet of Si $^+$  whose components lie a few  $\text{\AA}$  to the blue of Ly $\beta$ . The shorter of the two components is Raman-transformed to  $\lambda_{\text{air}} = 6362.35 \text{ \AA}$ , which unfortunately coincides with the collisionally excited [O I] line at  $6363.78 \text{ \AA}$ . The longer component is transformed to  $6480.81 \text{ \AA}$  in a region that is clear of any strong nebular lines. Wavelengths for these lines are based on energy levels from Martin & Zalubas (1983), with an estimated precision of  $0.1 \text{ cm}^{-1}$ , which gives an uncertainty in the optical wavelengths  $\lambda_2$  of  $0.04 \text{ \AA}$ .

The total cross-section for the off-resonance  $1s \rightarrow 3p$  transition in H $^0$  is calculated in § 2 of Chang et al. (2015) from second order time-dependent perturbation theory. Results are presented in the upper panel of Figure 1 of that paper in terms of a Doppler velocity factor  $\Delta V_1$ , which in the notation of the current paper is

$$\Delta V_1 = c \left( \frac{\lambda_1}{\lambda(\text{Ly}\beta)} - 1 \right). \quad (3)$$

The observed Raman-scattered wings of H $\alpha$  that are analyzed below are typically within  $\Delta\lambda_2 \sim \pm 100 \text{ \AA}$  of the line core. It is therefore convenient to define a dimensionless wavelength in the optical domain as

$$x = \frac{\lambda_2 - \lambda(\text{H}\alpha)}{100 \text{ \AA}}, \quad (4)$$

which corresponds to  $x \approx \Delta V_1 / 714 \text{ km s}^{-1}$  in the FUV domain. The total cross section in the range  $0.4 < |x| < 2.3$  can then be fit as follows:

$$\frac{\sigma}{10^{-21} \text{ cm}^2} = \begin{cases} 0.2186x^{-2} - 0.0344x^{-1} - 0.0054 & \text{if } x < 0 \\ 0.2367x^{-2} - 0.0187x^{-1} + 0.0041 & \text{if } x > 0 \end{cases} \quad (5)$$

Note that separate fits are given for the blue ( $x < 0$ ) and red ( $x > 0$ ) wings of H $\alpha$  since the cross section, although approximately Lorentzian, is not exactly symmetric, being stronger on the blue side (by about 10% for  $x = \pm 1$ ).

The fraction of all  $1s \rightarrow 3p$  excitations that result in Raman scattering to an optical photon is given by the branching ratio,  $f_{H\alpha}$ , with the remaining fraction,  $1 - f_{H\alpha}$ , resulting in elastic Rayleigh scattering in which the photon remains in the FUV domain. The results for  $f_{H\alpha}$  are also shown in Figure 1 of Chang et al. (2015) and can be fit as follows in the range  $|x| < 5$ :

$$f_{H\alpha} = 0.2238 + 0.0363x + 0.0024x^2 . \quad (6)$$

The relative accuracy of all these fits is better than 1% within the stated range (corresponding to  $\sigma \approx 10^{-22} \text{ cm}^2$  to  $10^{-21} \text{ cm}^2$ ), which is perfectly adequate for the purposes of this paper. Note that the branching ratio increases with  $x$ , which means that the product  $\sigma f_{H\alpha}$  is stronger on the red side of  $H\alpha$ .

### 3. SPECTRAL MAPPING OF RAMAN WINGS

The principal observational dataset used in this paper is the imaging spectroscopy mosaic of the inner Orion Nebula (Weilbacher et al. 2015; Mc Leod et al. 2015) obtained with the MUSE spectrograph (Bacon et al. 2010, 2014) on the VLT. The entire datacube covers the wavelength range 4595 to 9366 Å but we concentrate mainly on the range 6300 to 6800 Å, where the spectral resolving power is  $R \approx 2500$ , corresponding to an instrumental linewidth (FWHM) of  $\delta\lambda \approx 2.4 \text{ \AA}$ , which is sampled at  $1.25 \text{ \AA pix}^{-1}$  and then resampled to  $0.85 \text{ \AA pix}^{-1}$  for the final calibrated cube (see § 2 of Weilbacher et al. 2015). The observed field is shown by the white rectangle in Figure 2(a) and includes the entire inner Huygens region of the nebula, which accounts for roughly half of the total radio continuum flux from the H II region (Subrahmanyan et al. 2001). The full datacube is a mosaic that combines observations from 30 separate pointings, with a pixel size of  $0.2 \times 0.2''$ .

#### 3.1. Raman scattered $H\alpha$ wings

Extended wings to the  $H\alpha$  line are detected over the entire map, but they are particularly prominent in the six regions marked as white boxes in Figure 2(b). These are all bar-like features (O'Dell & Yusef-Zadeh 2000; García-Díaz & Henney 2007), which correspond to filamentary ionization fronts. Extracted MUSE spectra around the  $H\alpha$  line for each of these regions are shown in Figure 3. All regions show broad wings to the  $H\alpha$  line extending from 6300 to 6700 Å, which are consistent with the higher spectral resolution ( $R = 7000$ ) results of Dopita et al. (2016) for the region indicated by a dashed box in Figure 2(b). The continuum is interpolated under the wings by fitting a second-order polynomial to clean regions of the spectra in the ranges 6070 Å to 6225 Å and 6760 Å to 6820 Å, as shown by the lower edge of the gray shading for each spectrum. The continuum is a combination of Paschen recombination emission from hydrogen, which increases to the red, and dust-scattered starlight and two-photon hydrogen emission, which both increase to the blue. The combined  $F_\lambda$  is approximately flat for all regions except the Orion Bar, where dust scattering of the nearby star  $\theta^2$  Ori A dominates, resulting in a blueward rise. All of these continuum processes are expected to be smooth on a 100 Å scale,<sup>1</sup> but nonetheless the systematic uncertainties in the continuum interpolation is an important factor that limits the precision of the Raman wing measurements.

#### 3.2. Raman scattered FUV absorption lines

A prominent feature of all the spectra in Figure 3 is a pair of absorption notches in the red wing at 6633 Å and 6664 Å, which closely correspond to the wavelengths expected for the Raman-scattered transformation of the O I resonance lines at 1027 Å and 1028 Å listed in Table 1. After correcting for instrumental broadening, the FWHM of the 6633 Å feature is  $\approx 2.5 \text{ \AA}$ , which would correspond to a velocity width of  $115 \text{ km s}^{-1}$  if it were an optical absorption line. However, taking into account the wavelength transformation during Raman scattering (eq. [2]), the true velocity width of the FUV line is  $18 \text{ km s}^{-1}$ . The absorption depth of the features is roughly 50% with respect to the Raman-scattered wing at adjacent wavelengths, but is much lower with respect to the total continuum emission. The same spectral features are also visible in the Dopita et al. (2016) spectra but are not commented on by those authors. The 6664 Å feature is partially blended with the [Ni II] 6666.8 Å nebular emission line in the MUSE spectra, but these are better resolved in the higher resolution Dopita et al. spectra. Archival Keck HIRES observations of this feature at an even higher spectral resolution are presented below in § 4. The identification of these two FUV absorption lines in the optical spectrum is incontestable proof of a Raman scattering origin for the broad  $H\alpha$  wings.

There is also evidence for a weak absorption feature in the blue wing at 6481 Å, corresponding to the Si II absorption line at 1024 Å. However, the blue wing is much less clean than the red wing, partly due to telluric absorption and airglow emission (see below), which makes the identification uncertain. The Raman wings show some other weak features that remain unidentified, the strongest of which is an apparent broad ( $\approx 5 \text{ \AA}$ ) absorption feature at 6494 Å, while additional narrower features are seen at

<sup>1</sup> The only exception is the dust-scattered  $H\alpha$  line from the stellar photospheres and winds, but this is confined within  $\pm 30 \text{ \AA}$  of the rest wavelength (see Fig. 2 of Simón-Díaz et al. 2006) and so does not affect the Raman wings, which are broader than that.

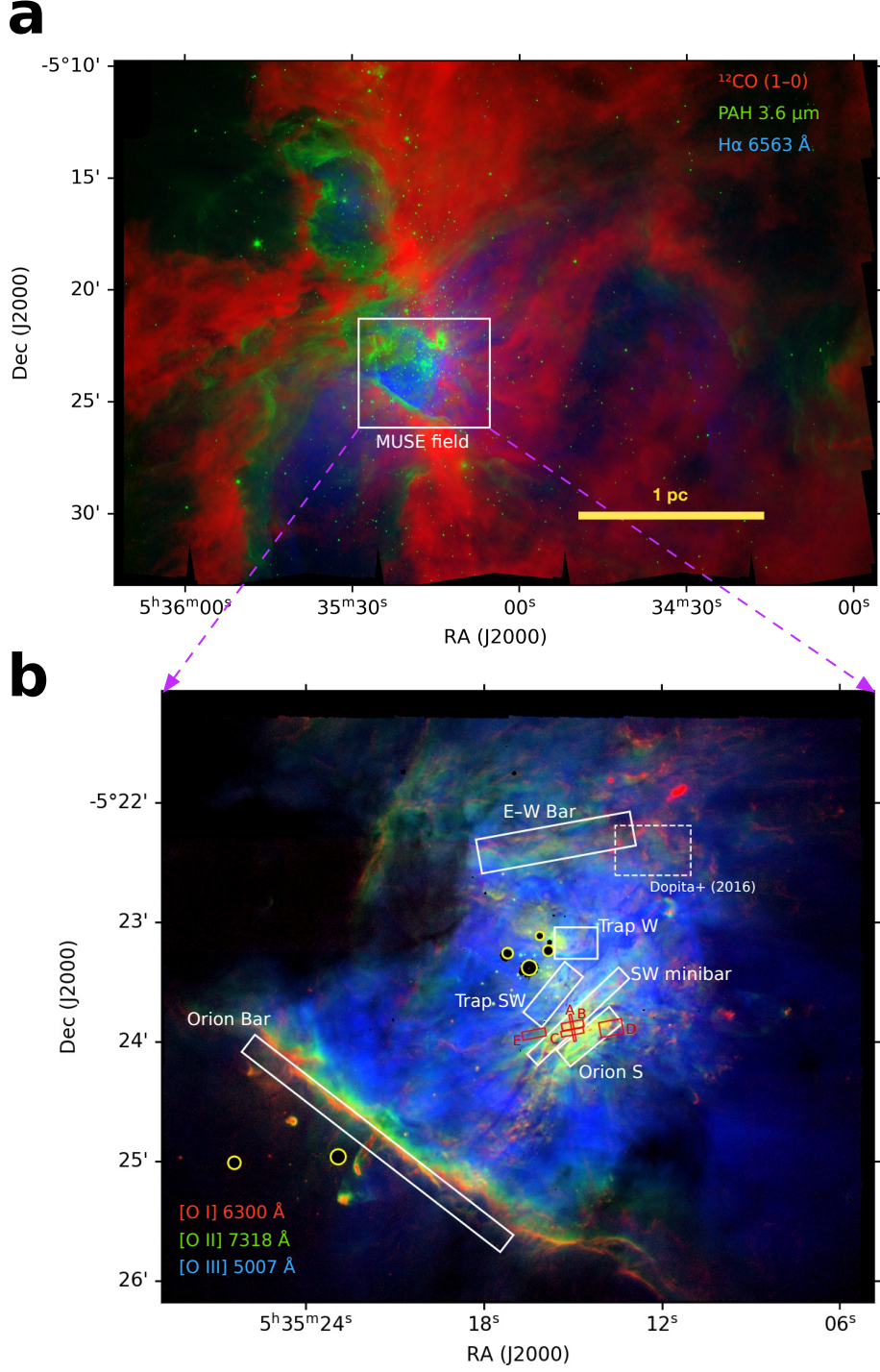


**Figure 2.** (a) Panoramic view of the Orion Nebula region on parsec scales. Red channel of background image shows  $^{12}\text{CO}$  emission from dense molecular gas (Carma-NRO Orion Survey, Kong et al. 2018). Green channel shows near-infrared continuum from PAH grains in neutral gas (Spitzer Orion Survey, Megeath et al. 2012). Blue channel shows optical H $\alpha$  emission from ionized gas (WFI camera on ESO 2.2 m La Silla, Da Rio et al. 2009). The white box shows the field of view observed with MUSE. (b) Locations within the nebula of the extraction regions for the MUSE spectra shown in Figure 3 (white boxes) and the Keck HIRES spectra shown in Figure 8 (red boxes). The region of the spectrum obtained in Dopita et al. (2016) is shown by the dashed box. Background image shows oxygen emission lines extracted from the MUSE data cube: [O I]  $\lambda 6300 \text{ \AA}$  (red channel), which traces ionization fronts and shocks in neutral gas; [O II]  $\lambda 7318 \text{ \AA}$  (green channel), which traces the outer layers of the photoionized nebula; and [O III]  $\lambda 5007 \text{ \AA}$  (blue channel), which traces the highly ionized interior of the nebula.

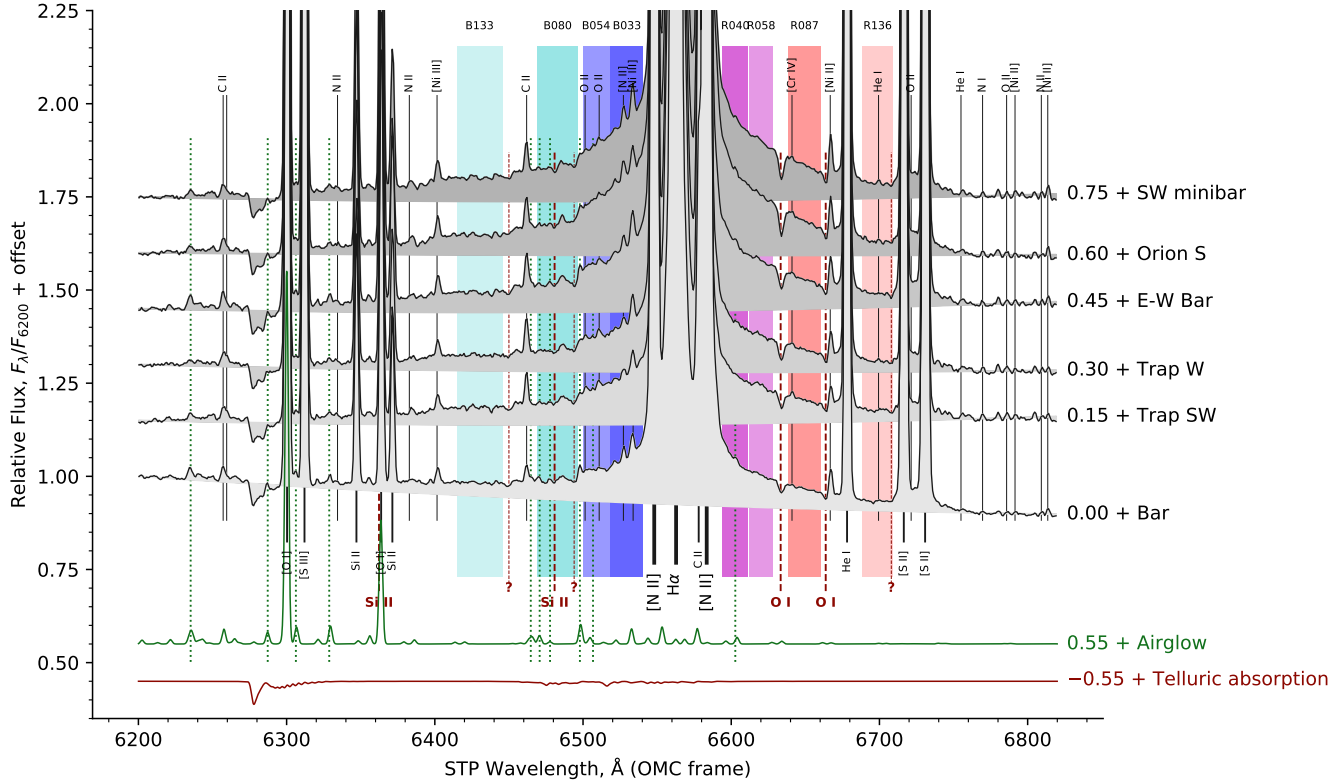


**Figure 3.** MUSE spectra of the Orion Nebula centered on the H $\alpha$  line, showing the broad Raman-scattered wings. Spectra are shown for the regions outlined by white boxes in Figure 2 and were extracted from the datacubes of Weilbacher et al. (2015). All spectra are normalized to the continuum at 6200 Å and are offset vertically as labelled at right. Emission line identifications are shown by solid vertical lines, labelled above for weak lines and below for stronger lines. Wavelengths of Raman-scattered O I and Si II absorption lines from Table 1 are shown by red dashed vertical lines, labelled in bold font below, together with unidentified candidate absorption features marked with “?”. Dotted lines show night sky lines identified in the Dark Bay region of the nebula. At the bottom of the figure are shown the theoretical upper-atmosphere airglow spectrum (green line) and telluric molecular absorption spectrum (red line), as calculated from the Cerro Paranal Advanced Sky Model (Noll et al. 2012; Moehler et al. 2014).

6450 Å and 6708 Å (all marked with “?” in Figure 3). It is not clear if these are truly absorption features or whether they are simply gaps between very weak blended emission lines.

### 3.3. Definition of observational Raman bands in the red and blue wings

In order to study the spatial distribution of the Raman-scattered wings, it is convenient to define a series of broad bands on the blue and red sides, which are listed in Table 2 and shown as blue and red shaded vertical stripes in Figure 3. Four bands are defined in each wing, spanning a range in  $|\Delta\lambda_2|$  from about 30 Å to 150 Å. The lower limit of this range is determined by overlap with the strong nebular [N II] emission lines, while the upper limit is due the [S II] lines on the red side, combined with the Raman wings becoming too weak to measure. The mean H $^0$  Ly $\beta$  cross section corresponding to each band (eq. [5]) is also given in the table, varying between about  $10^{-22}$  cm $^2$  and  $2 \times 10^{-21}$  cm $^2$ .

The bands are chosen so as to avoid the strongest contaminating lines wherever possible, but some small contamination is unavoidable, as listed in the rightmost column of the table. The contamination comes from two sources: weak nebular emission lines (indicated by solid vertical lines in Figure 3) and additionally from the line absorption and emission of the Earth’s atmosphere. Two complementary methods were used to investigate this latter effect. First, the datacube was inspected to identify lines with roughly uniform brightness across the entire map. In particular, any line that is as strong in the Dark Bay region as it is in Orion S is unlikely to come from the nebula itself. Such lines are indicated by vertical dotted lines in Figure 3 and some are listed in Table 2. Second, ESO’s SkyCalc tool<sup>2</sup> was used to predict theoretical emission and absorption spectra for the atmosphere above

<sup>2</sup> <http://www.eso.org/sci/software/pipelines/skytools/skycalc>

**Table 2.** Wavelength bands used for Raman wing extraction

	Band	$\langle \Delta\lambda_2 \rangle, \text{\AA}$	$\lambda_{\min}, \text{\AA}$	$\lambda_{\max}, \text{\AA}$	$f_{H\alpha}$	$\langle \sigma_\lambda \rangle, 10^{-21} \text{ cm}^2$	Contamination
	(1)	(2)	(3)	(4)	(5)	(6)	(7)
Blue wing	B133	-132.8	6414.85	6445.45	0.180	0.144	
	B080	-79.5	6469.25	6496.45	0.196	0.378	Sky 6471, 6478, H <sub>2</sub> O
	B054	-53.6	6499.85	6517.70	0.205	0.802	O II? 6502, 6510, Sky 6507, H <sub>2</sub> O
	B033	-32.8	6518.55	6540.65	0.212	2.069	[N II] 6527.24, [Ni III] 6533.76, H <sub>2</sub> O
Red wing	R040	40.3	6594.20	6611.20	0.238	1.451	Sky 6603
	R058	57.7	6612.05	6628.20	0.244	0.695	
	R087	87.1	6638.40	6660.50	0.255	0.299	[Cr IV]? 6641
	R136	135.7	6688.55	6708.95	0.274	0.119	He I 6699

COLUMNS: (1) Name of band. (2) Mean wavelength displacement from H $\alpha$  rest wavelength. (3, 4) Upper and lower wavelength limits for the band. (5) Mean value of the H $\alpha$  branching ratio from virtual 3p levels (see equation [6]). (6) Mean value of Ly $\beta$  wing cross-section that can feed this band via Raman scattering (see equation [5]). (7) Nebular and telluric lines that may contaminate the band (see text for details).

the VLT at the time and airmass of the observations, convolved with the MUSE instrumental profile. The emission spectrum is dominated by upper-atmosphere airglow lines of OH (Osterbrock et al. 1996; Noll et al. 2012, 2014), shown in green in the figure, many of which can be seen to coincide with the empirically determined sky lines. The absorption spectrum is dominated by telluric lines of O<sub>2</sub> and H<sub>2</sub>O (Moehler et al. 2014; Smette et al. 2015). The strongest predicted absorption near H $\alpha$  is the O<sub>2</sub>  $\gamma$  band at 6280 Å, which is clearly seen in all the spectra, with an absorption depth of order 0.1, but lies well away from the Raman wings. The blue Raman wing is affected by weaker H<sub>2</sub>O bands at 6460 Å to 6600 Å with absorption depth < 0.01, as compared to the relative brightness of the Raman wings at those wavelengths, which is 0.05 to 0.1.

In summary, the nebular and telluric contamination introduces uncertainties of order 10% in the fluxes of the B033, B054, and B080 bands, with other bands being affected to a much lesser degree.

### 3.4. Spatial distribution of Raman band emission

Figure 4 shows maps of the six innermost Raman bands as two RGB images: the blue wing in panel a and the red wing in panel b. In each case, the channel sequence R, G, B is an inward progression towards line center, from the farther wings to the nearer wings. The maps are adaptively smoothed following the binary grid algorithm outlined in García-Díaz et al. (2018), which reduces the noise in the fainter regions at the cost of a reduced spatial resolution. The two maps are strikingly similar, indicating that the contamination of the blue wing (see previous section) is indeed a minor effect when integrated over an entire band.

To aid in the interpretation of the Raman wing maps, Figure 4c shows a combined view of mid-to-low-ionization oxygen emission lines, derived from the MUSE data cube. In blue is shown the [O II] 7318.39, 7319.99 Å doublet, which traces the outer 10% of the fully ionized emission. In green is shown the [O I] 6300.30 Å line, which principally traces partially ionized gas at the ionization front, but also shocks in neutral gas. In red is shown the fluorescent O I 8446.36 Å line, which traces fully neutral gas that is very close behind the ionization front. This image clearly illustrates that the neutral/molecular gas is organized in filaments, with bright ionization fronts on the side facing the high-mass Trapezium stars. This is most clearly seen in the Orion Bar, the linear emission feature to the south-east of the map, but analogous filaments are seen in all directions from the Trapezium (see also Figure 2b). A particularly complex region, with several partially overlapping filaments, lies between the Trapezium and the Orion S star formation region. This region shows the brightest Raman wing emission, suggesting that it contains the neutral gas with the highest incident FUV flux, presumably because it lies physically closest to the illuminating high-mass stars.

The spatial relation of the Raman-scattered wings to other emission lines is illustrated in Figure 4d, which shows the summed wing intensity over all 8 bands as a false color scale. This is compared with contours that show the ionization front, as traced by the collisionally excited [O I] line, and molecular gas, as traced by the optically thick <sup>12</sup>CO (1–0) line (Kong et al. 2018). In the Bar region, the Raman emission is clearly seen to be sandwiched between the ionization front and the molecular gas, conclusive evidence that it arises in the neutral zone of the PDR. In the Orion S region and around the Trapezium, there is not such a clear stratification between ionized, neutral, and molecular emission. This is due to two factors: first, the densities are higher, which shortens all length scales, and second, the geometry is not so edge-on, leading to a greater degree of superposition along the line of sight, as witnessed by the overlap of the [O I] and <sup>12</sup>CO contours. Nonetheless, even here there is evidence that the Raman emission tends to lie farther from θ<sup>1</sup> Ori C than the ionization front, particularly in the “SW minibar” region.

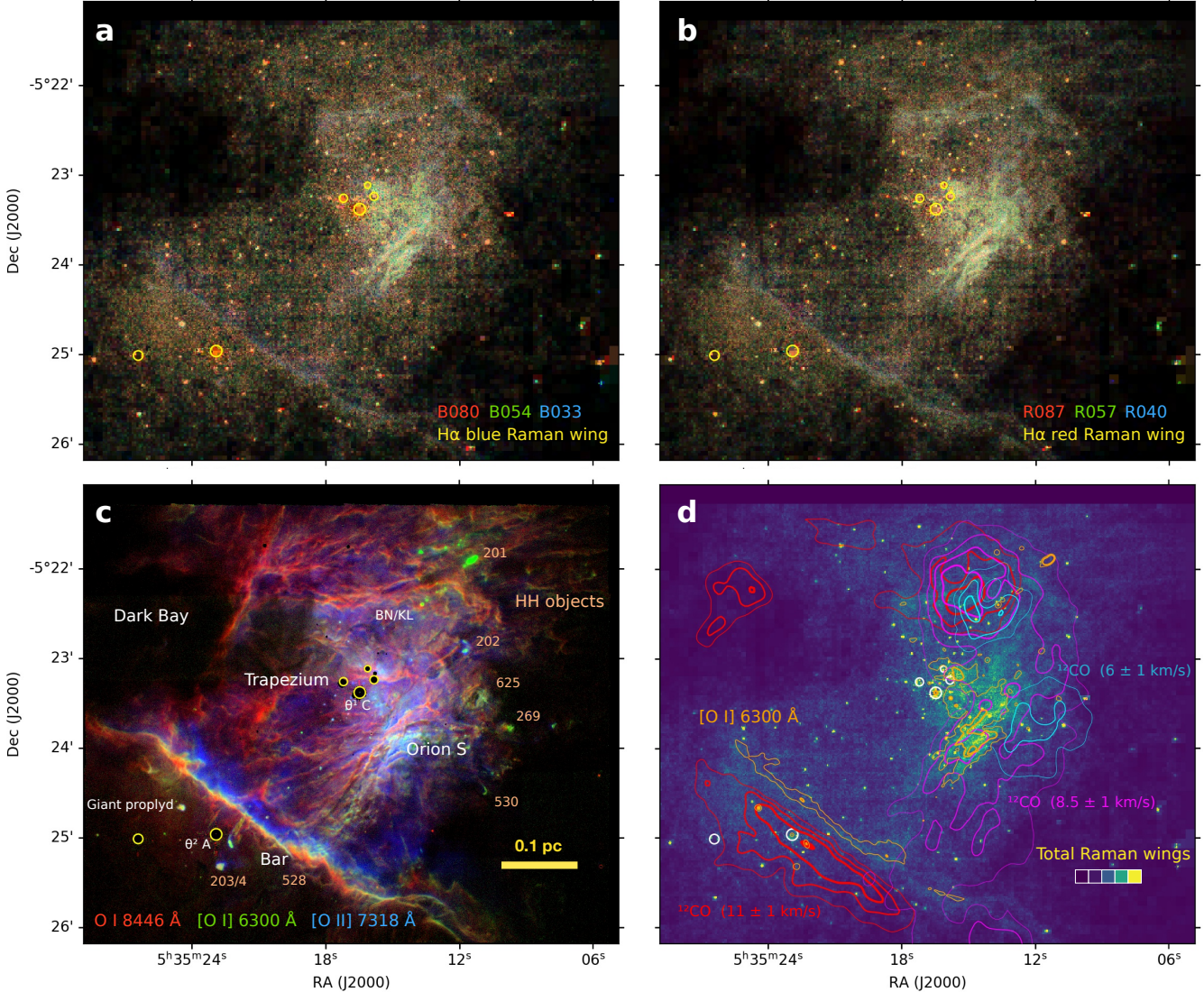


**Figure 4.** Spatial distribution of Raman-scattered wings of H $\alpha$ . (a) Three-color RGB image of bands in the blue wing: B080 (red channel), B054 (green), B033 (blue). All bands are continuum-subtracted and are multibinned at constant signal-to-noise (see text). Maximum brightness in the (red, green, blue) channels is  $(2.27, 3.89, 7.78) \times 10^{-9} \text{ erg s}^{-1} \text{ cm}^{-2} \text{ sr}^{-1} \text{ Å}^{-1}$ . The brightest stars are masked out and marked with yellow circles. Lower-mass stars are not masked and most appear as yellow/red dots. (b) Same as (a) but for bands in the red wing: R087 (red), R057 (green), R040 (blue). (c) Three-color RGB image of collisional and fluorescent oxygen emission lines that bracket the ionization front: O I  $\lambda$ 8446 Å (red), [O I]  $\lambda$ 6300 (green), [O II]  $\lambda\lambda$ 7318 Å (blue). Various features of the nebula are marked, including Herbig-Haro objects driven by jets from young stars. (d) Comparison of the total Raman wing intensity (blue-to-yellow false color image) with the [O I] emission that traces the ionization front (orange contours) and  $^{12}\text{CO}$  emission that traces molecular gas (red, purple, and blue contours for different LSR velocities as marked).

### 3.5. Emission profiles across the Orion Bar

Figure 5 shows spatial profiles across the Orion Bar of the Raman-scattered bands (upper panel), together with other emission lines and bands (lower panel). In keeping with the dominant tradition in the literature (e.g., Fig. 9 of van der Werf et al. 1996, Fig. 2 of Goicoechea et al. 2017), the molecular regions are shown on the left and the ionized regions on the right. Table 3 shows the positions, widths, and intensities of the peaks in each tracer, as determined by fitting a single Gaussian plus a linear background.

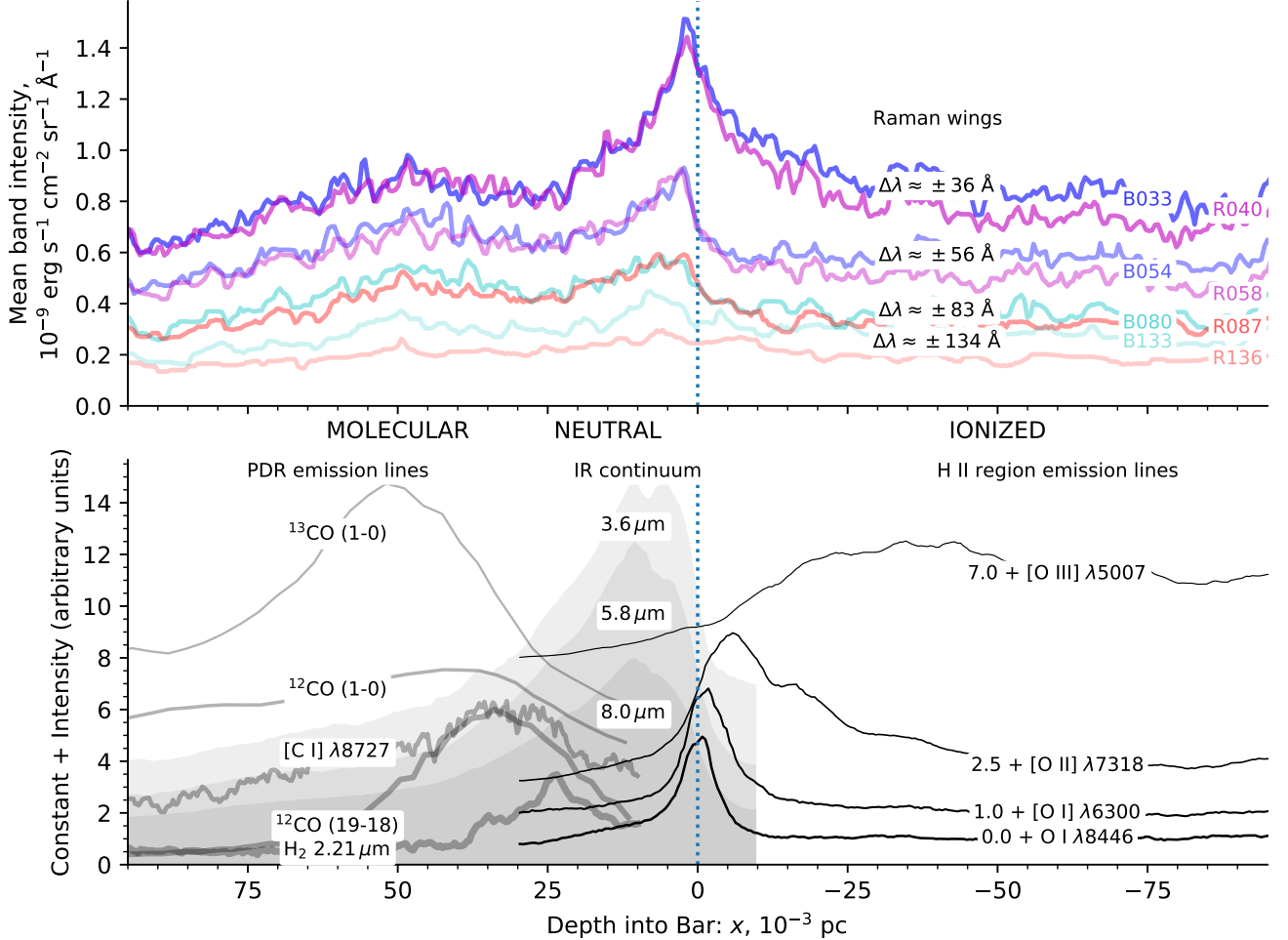


**Figure 5.** Spatial cut of continuum-subtracted  $\text{H}\alpha$  wing intensity across the Orion Bar (top panel). Matched red and blue wing bands are shown with the same color scheme as in Fig. 3. Bottom panel shows comparison with a variety of different tracers of molecular, neutral, and ionized material. Optical lines are from VLT MUSE (Weilbacher et al. 2015), infrared continuum bands are from Spitzer IRAC (Megeath et al. 2012), CO lines are from Carma-NRO (Kong et al. 2018) and Herschel PACS (Parikka et al. 2018),  $\text{H}_2$  near-infrared line is from VLT HAWK-I (Kissler-Patig et al. 2008). Ultraviolet photons are incident from the right hand side and the vertical dotted line indicates the ionization front, defined as the peak of the fluorescent  $\text{O I}$  emission. The profiles are the median values over a slit width of  $75''$ , centered on the ICRS equatorial coordinates  $\alpha = 83.8419^\circ$ ,  $\delta = -5.4113^\circ$  and oriented at a position angle of  $141.5^\circ$ . Distances from the ionization front are given in mpc where  $1'' \approx 1.9$  mpc for an assumed distance of  $(388 \pm 5)$  pc (Kounkel et al. 2017).

### 3.5.1. Lines from ionized gas and the ionization front

The ionization stratification at the edge of the H II region is clearly seen in the distribution of the  $[\text{O III}]$ ,  $[\text{O II}]$ ,  $[\text{O I}]$ , and  $\text{O I}$  lines. The peak in  $[\text{O I}]$  emissivity (excited by collisions between electrons and neutral oxygen atoms) is expected to occur at a hydrogen ionization fraction of 50% (Henney et al. 2005), which is displaced by  $x_0 \approx -1.7$  mpc from the peak of the  $\text{O I}$  fluorescent line. This latter should correspond to an absorption optical depth of approximately unity in the FUV pumping lines, such as those listed in Table 1 (see § 5 of Walmsley et al. 2000), corresponding to a neutral hydrogen column density of  $N(\text{H}^0) \approx 10^{19} \text{ cm}^{-2}$  and therefore an average volume density of  $n(\text{H}^0) = N(\text{H}^0)/|x_0| \approx 2000 \text{ cm}^{-3}$ . This value is similar to the peak electron density on the fully ionized side of the ionization front:  $n_e \approx 3000 \text{ cm}^{-3}$ , measured from the  $[\text{S II}] 6717/6731$  ratio (e.g. O'Dell et al. 2017), which occurs at  $x \approx -7$  mpc, close to the peak in the  $[\text{O II}]$  emission. Therefore, the *total* hydrogen density is roughly constant over the transition between a predominantly ionized state and predominantly neutral state. Note that the apparent width of this transition (for instance, the FWHM of the  $[\text{O I}]$  peak  $\approx 9$  mpc) is much larger than predicted by atomic physics, which is probably due to spatial irregularities in the ionization front, as discussed in detail in § 5.1 below.

**Table 3.** Peaks in emission profiles across the Orion Bar

Emission type and units (1)	Line or Band (2)	$x_0$ , mpc (3)	$\delta x$ , mpc (4)	$I$ (Peak) (5)	$I$ (BG) (6)
H II region emission lines Peak and BG: $\int I_\lambda d\lambda$ , $10^{-6}$ erg s $^{-1}$ cm $^{-2}$ sr $^{-1}$	[O III] $\lambda 5007$	-32.1	45	13.059	$11.642 \pm 5.605$
	[O II] $\lambda 7318$	-9.4	25	0.882	$0.232 \pm 0.026$
	[OI] $\lambda 6300$	-1.7	9	0.152	$0.045 \pm 0.001$
	O I $\lambda 8446$	0.0	8	0.226	$0.071 \pm 0.000$
Raman bands Peak and BG: $I_\lambda$ , $10^{-9}$ erg s $^{-1}$ cm $^{-2}$ sr $^{-1}$ Å $^{-1}$	B033	0.8	20	0.455	$0.858 \pm 0.007$
	R040	1.8	18	0.480	$0.815 \pm 0.023$
	B054	5.0	9	0.233	$0.641 \pm 0.009$
	R058	5.5	11	0.285	$0.591 \pm 0.017$
	B080	7.1	11	0.136	$0.437 \pm 0.013$
	R087	7.1	15	0.178	$0.393 \pm 0.017$
	B133	6.7	10	0.128	$0.302 \pm 0.004$
	R136	3.1	27	0.072	$0.198 \pm 0.007$
IRAC bands Peak and BG: $I_\nu$ , GJy sr $^{-1}$	3.6 $\mu$ m	11.6	21	0.200	$0.182 \pm 0.018$
	5.8 $\mu$ m	12.8	23	1.702	$0.966 \pm 0.073$
	8.0 $\mu$ m	13.9	24	4.866	$2.622 \pm 0.119$
PDR emission lines Peak and BG: $\int I_\lambda d\lambda$ , median normalized	H <sub>2</sub> 2.21 $\mu$ m	23.6	19	0.169	$0.997 \pm 0.002$
	<sup>12</sup> CO (19–18)	33.8	32	3.930	$0.399 \pm 0.001$
	[CI] $\lambda 8727$	37.7	30	0.495	$0.854 \pm 0.122$
	<sup>12</sup> CO (1–0)	41.1	44	0.472	$0.746 \pm 0.173$
	<sup>13</sup> CO (1–0)	49.8	33	0.891	$0.823 \pm 0.112$

NOTE—Results of fitting a single Gaussian plus linear background to the brightness profiles shown in Figure 5 (see figure caption for references). Columns: (1) Type of tracer and surface brightness units for the values given in columns 5 and 6. (2) Specific emission line or continuum band. (3) Position of fitted Gaussian relative to ionization front. (4) FWHM of fitted Gaussian. (5) Peak intensity of fitted Gaussian, with brightness units given in column 1. (6) Intensity of fitted background at position  $x_0 \pm \delta x$ .

### 3.5.2. Spatial profiles of the Raman bands

Unlike the optical emission lines, the Raman wing bands (upper panel of Fig. 5) all show peaks at positive values of  $x$ , corresponding to fully neutral gas in the PDR. There is a very close correspondence between corresponding pairs of blue and red bands: B033 with R040, B054 with R058, and B080 with R087. However, there is a systematic tendency for the blue band intensity to be slightly higher than its red counterpart on the ionized side (negative values of  $x$ ), which is probably due to contamination by nebular emission lines, as listed in column 7 of Table 2. There is a clear tendency for the peak in the brightness profile to progress towards greater depths into the neutral gas as one moves to wavelengths farther from the H $\alpha$  line center, which is quantitatively confirmed by the Gaussian fits in Table 3. If the peak emission occurs for a Ly $\beta$  wing optical depth of  $\tau \approx 1$  for each band, then the displacement from the ionization front should vary as  $x_0 \approx (n\langle\sigma_\lambda\rangle)^{-1}$ , where  $n$  is the neutral hydrogen density in the PDR and  $\langle\sigma_\lambda\rangle$  is the Ly $\beta$  wing cross section for the FUV wavelengths that pump each band, which is given in column 6 of Table 2. In Figure 6, this relationship is tested under the assumption that  $n$  is constant over the depth range 2 mpc to 8 mpc, where it can be seen that a PDR density of order  $n \sim 10^5$  cm $^{-3}$  is required to fit the observations. A systematic uncertainty of 10% of the width of each emission peak is assigned to the  $x_0$  values, which has the largest relative impact on the near-wing bands: B033 and R040. As a result, it is the B054 and R058 bands that are the most reliable indicators, yielding  $n = 8.5 \times 10^4$  cm $^{-3}$  (dotted line). The bands in the farther wings fall below this curve, significantly so for B133 and R136, but this can be understood as due to two factors. First, the finite total H $^0$  column through the PDR means that the wings will become optically thin for a sufficiently low  $\langle\sigma_\lambda\rangle$ , in which case  $\tau = 1$  can no longer hold. Second, competition with dust grains for the absorption of FUV photons will become significant when  $\langle\sigma_\lambda\rangle < \sigma_{\text{dust}}$ . These issues are discussed further in § 5.

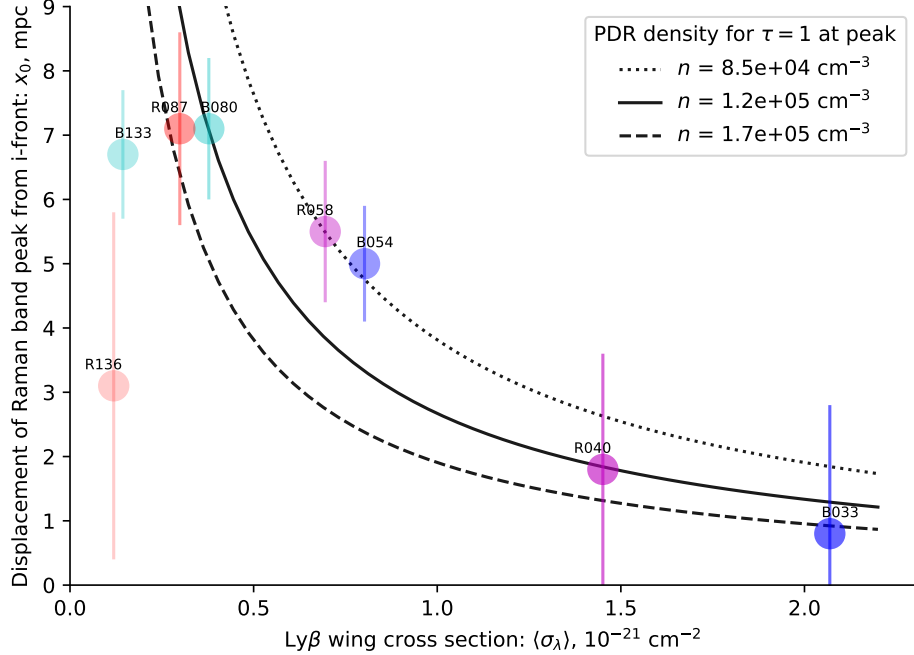


**Figure 6.** Displacement from the ionization front of the emission peak in each Raman band (column 3 of Table 3), plotted as a function of the cross-section of the Ly $\beta$  wing (column 6 of Table 2). Color scheme is as in Fig. 3 with error bars showing 10% of the peak FWHM (column 4 of Table 3). Black lines show a simple model in which the peaks occur at  $\tau = 1$  for 3 different constant neutral hydrogen densities, as indicated in the legend.

**Table 4.** Fit parameters from Gaussian line fits

Region	OI			Ni II		
	A	V	$\sigma$	A	V	$\sigma$
A						
B						
C						
D						
E						

### 3.5.3. Other PDR tracers

In summary,

The 21 cm H I line (van der Werf et al. 2013) probes deeper zones of the PDR than the Raman scattering, since it peaks at the position of the H<sub>2</sub> emission.

## 4. HIGH-RESOLUTION SPECTROSCOPY OF RAMAN-SCATTERED O I 1028 Å

Keck HIRES spectra described in Henney & O'Dell (1999) and Bally et al. (2000). The spectrum I use is of HH 529 base region in Orion South. Published results from these data have concentrated on strong nebular lines, but here I use a small section of the spectrum in the range 6660 Å to 6670 Å for reasons which will become apparent.

## 5. DISCUSSION

Location of H<sup>0</sup>. Neutral veil in front of nebula has column density of  $1.6 \times 10^{21} \text{ cm}^{-2}$  and  $3.2 \times 10^{21} \text{ cm}^{-2}$  in components A and B (Abel et al. 2006).

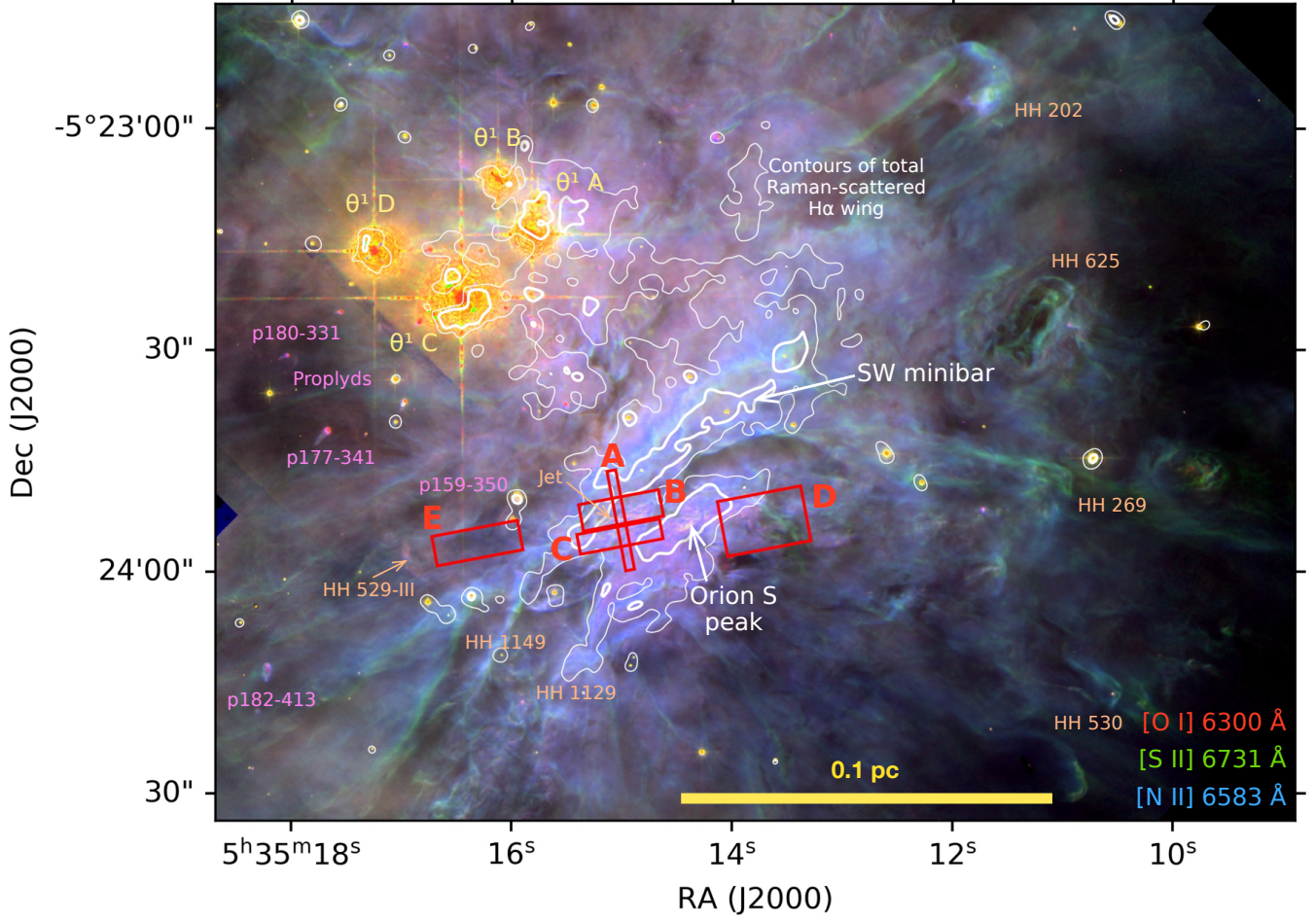


**Figure 7.** Zoom on Trapezium and Orion South region, showing regions of extracted Keck spectra.

### 5.1. Structure of the Orion Bar

Geometry of bar: in Henney et al. (2005) I pointed out that a diverging cylindrical geometry is necessary to explain the sharp peak in the [N II] emissivity seen at the ionization front. It has been apparent since O'Dell & Yusef-Zadeh (2000) that the nebula contains many bar-like features.

Salgado et al. (2016) had found low dust cross-section in Orion Bar PDR, but there are loopholes. First, they assume plane-parallel geometry with exactly edge-on viewing angle, while in reality it is a roughly cylindrical filament. Second, they ignore scattering, see Watson et al. (1998). Also, density increase with depth

### 5.2. Rival explanations for the 6633, 6664 lines

No stellar absorption lines there (Simón-Díaz et al. 2006). Too broad to be atomic or ionic absorption line. So strong it would have to be a resonance line. Could be solid-state feature, such as DIBs, but at that wavelength there are only weak features that are seen at very high extinction columns. Would have to be imprinted during back-scattering so as not to be seen in the stellar spectra.

### 5.3. Miscellany

The effective resolving power of the optical spectrograph is multiplied by 6.4 for the FUV domain.

The O I lines should be in absorption in the spectrum seen by the Raman scatterers.

Non-equilibrium PDRs (Stoerzer & Hollenbach 1998; Bertoldi & Draine 1996). Recent models from Bron et al. (2018).

C I emission from non-steady PDRs (Stoerzer et al. 1997) (fine structure lines, but maybe optical lines would be similar).

Escalante et al. (1991) model the far-red [C I] line as recombination of C<sup>+</sup>.

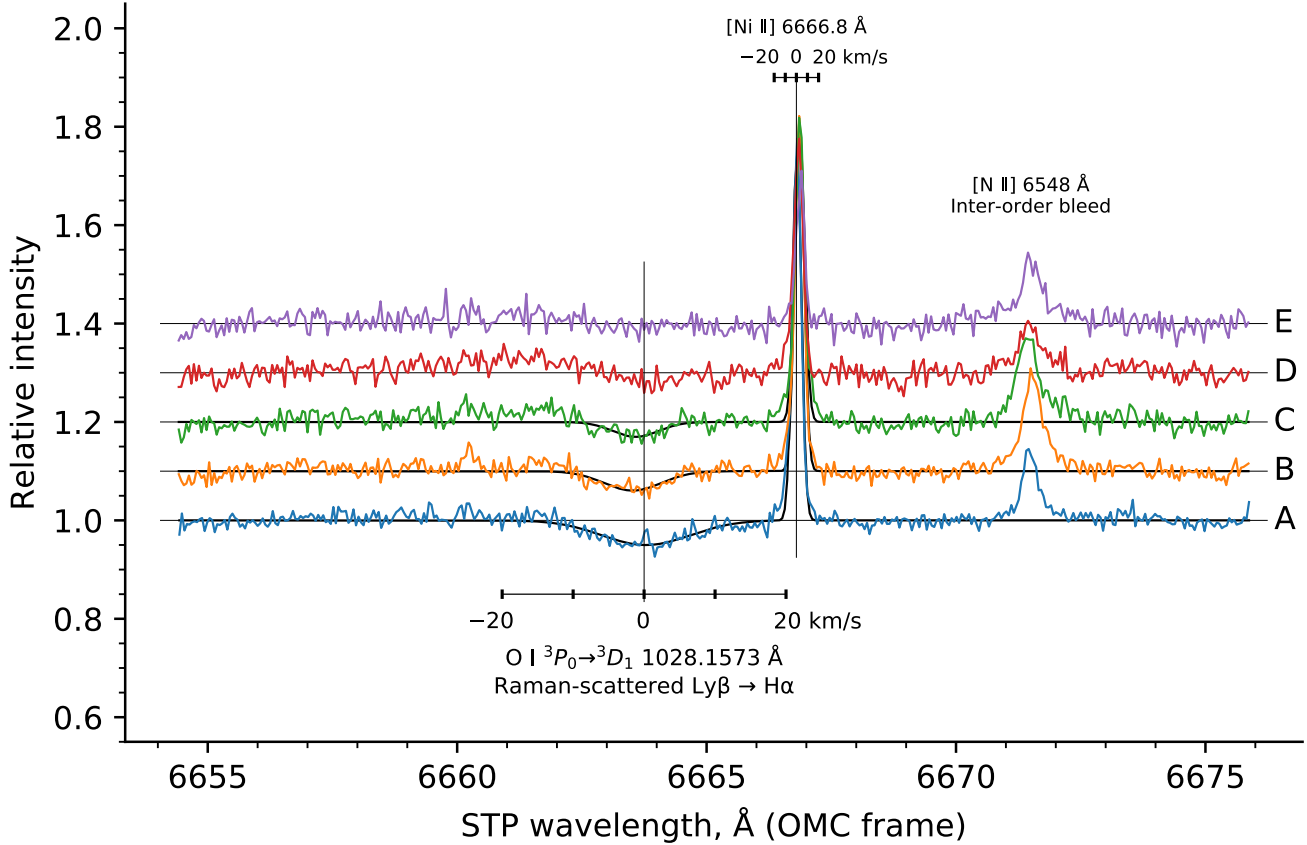


**Figure 8.** Keck HIRES spectra of Raman-scattered O I absorption line for five regions in Orion South. Wavelengths are given on an air scale and in the rest-frame of the Orion Molecular Cloud, as defined by the peak velocity of  $^{13}\text{CO}$ .

O VI 1037.62, 1031.93 absorption line in wind. No evidence for a blue absorption edge at  $V = 1200 \text{ km s}^{-1}$ , which would be at  $\lambda_2 = 6649 \text{ \AA}$ , right in middle of R087 band.

Even for high PDR optical depth, no multiple Raman scattering will occur since the population of 2s is very small and the post-scattered photons have insufficient energy to excite any transitions from 1s.

#### ACKNOWLEDGMENTS

This work has made use of the Atomic Line List<sup>3</sup> (Van Hoof 2018).

#### REFERENCES

- Abel, N. P., Ferland, G. J., O'Dell, C. R., Shaw, G., & Troland, T. H. 2006, ApJ, 644, 344, doi: [10.1086/500819](https://doi.org/10.1086/500819)
- Bacon, R., Accardo, M., Adjali, L., et al. 2010, in Society of Photo-Optical Instrumentation Engineers (SPIE) Conference Series, Vol. 7735, Proc. SPIE, 773508, doi: [10.1117/12.856027](https://doi.org/10.1117/12.856027)
- Bacon, R., Vernet, J., Borisova, E., et al. 2014, The Messenger, 157, 13
- Bally, J., O'Dell, C. R., & McCaughrean, M. J. 2000, AJ, 119, 2919, doi: [10.1086/301385](https://doi.org/10.1086/301385)
- Bertoldi, F., & Draine, B. T. 1996, ApJ, 458, 222, doi: [10.1086/176805](https://doi.org/10.1086/176805)
- Bron, E., Agúndez, M., Goicoechea, J. R., & Cernicharo, J. 2018, arXiv e-prints. <https://arxiv.org/abs/1801.01547>
- Chang, S.-J., Heo, J.-E., Di Mille, F., et al. 2015, ApJ, 814, 98, doi: [10.1088/0004-637X/814/2/98](https://doi.org/10.1088/0004-637X/814/2/98)
- Clegg, R. E. S., Miller, S., Storey, P. J., & Kisielius, R. 1999, A&AS, 135, 359, doi: [10.1051/aas:1999178](https://doi.org/10.1051/aas:1999178)

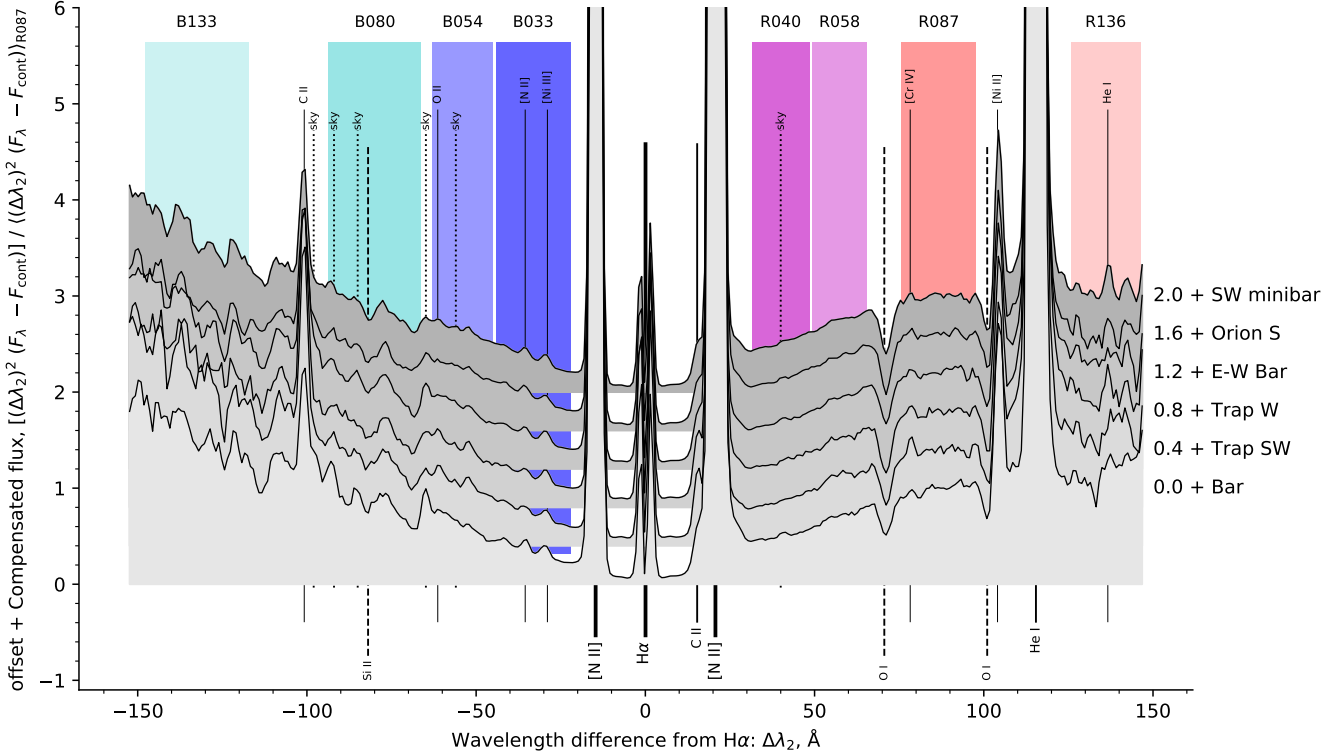


**Figure 9.** Same as Fig. 3 but with  $F_\lambda$  multiplied by  $(\Delta\lambda_2)^2$  and zoomed in on the Raman wing wavelengths. The spectrum is normalized by the average flux in the R087 band and each region is offset vertically by a constant value, as indicated at right. In this presentation, optically thin Raman scattering of a flat FUV spectrum should give a constant value, which for the Orion data is only seen in the R087 and R136 bands.

- Da Rio, N., Robberto, M., Soderblom, D. R., et al. 2009, ApJS, 183, 261, doi: [10.1088/0067-0049/183/2/261](https://doi.org/10.1088/0067-0049/183/2/261)
- Dicker, S. R., Mason, B. S., Kornget, P. M., et al. 2009, ApJ, 705, 226, doi: [10.1088/0004-637X/705/1/226](https://doi.org/10.1088/0004-637X/705/1/226)
- Dopita, M. A., Nicholls, D. C., Sutherland, R. S., Kewley, L. J., & Groves, B. A. 2016, ApJL, 824, L13, doi: [10.3847/2041-8205/824/1/L13](https://doi.org/10.3847/2041-8205/824/1/L13)
- Escalante, V., Sternberg, A., & Dalgarno, A. 1991, ApJ, 375, 630, doi: [10.1086/170225](https://doi.org/10.1086/170225)
- Foster, J. B., & Goodman, A. A. 2006, ApJL, 636, L105, doi: [10.1086/500131](https://doi.org/10.1086/500131)
- García-Díaz, M. T., & Henney, W. J. 2007, AJ, 133, 952, doi: [10.1086/510621](https://doi.org/10.1086/510621)
- García-Díaz, M. T., Steffen, W., Henney, W. J., et al. 2018, MNRAS, 479, 3909, doi: [10.1093/mnras/sty1590](https://doi.org/10.1093/mnras/sty1590)
- Goicoechea, J. R., Pety, J., Cuadrado, S., et al. 2016, Nature, 537, 207, doi: [10.1038/nature18957](https://doi.org/10.1038/nature18957)
- Goicoechea, J. R., Cuadrado, S., Pety, J., et al. 2017, A&A, 601, L9, doi: [10.1051/0004-6361/201730716](https://doi.org/10.1051/0004-6361/201730716)
- Green, D. A. 1991, MNRAS, 253, 350, doi: [10.1093/mnras/253.2.350](https://doi.org/10.1093/mnras/253.2.350)
- Green, D. A., & Padman, R. 1993, MNRAS, 263, 535, doi: [10.1093/mnras/263.2.535](https://doi.org/10.1093/mnras/263.2.535)

- Greisen, E. W., Calabretta, M. R., Valdes, F. G., & Allen, S. L. 2006, A&A, 446, 747, doi: [10.1051/0004-6361:20053818](https://doi.org/10.1051/0004-6361:20053818)
- Henney, W. J., Arthur, S. J., Williams, R. J. R., & Ferland, G. J. 2005, ApJ, 621, 328, doi: [10.1086/427491](https://doi.org/10.1086/427491)
- Henney, W. J., & O'Dell, C. R. 1999, AJ, 118, 2350, doi: [10.1086/301087](https://doi.org/10.1086/301087)
- Ivanov, T. I., Salumbides, E. J., Vieitez, M. O., et al. 2008, MNRAS, 389, L4, doi: [10.1111/j.1745-3933.2008.00507.x](https://doi.org/10.1111/j.1745-3933.2008.00507.x)
- Kissler-Patig, M., Pirard, J. F., Casali, M., et al. 2008, A&A, 491, 941, doi: [10.1051/0004-6361:200809910](https://doi.org/10.1051/0004-6361:200809910)
- Kong, S., Arce, H. G., Feddersen, J. R., et al. 2018, ApJS, 236, 25, doi: [10.3847/1538-4365/aaabfc](https://doi.org/10.3847/1538-4365/aaabfc)
- Kounkel, M., Hartmann, L., Loinard, L., et al. 2017, ApJ, 834, 142, doi: [10.3847/1538-4357/834/2/142](https://doi.org/10.3847/1538-4357/834/2/142)
- Marinov, D., Booth, J. P., Drag, C., & Blondel, C. 2017, Journal of Physics B Atomic Molecular Physics, 50, 065003, doi: [10.1088/1361-6455/aa5a88](https://doi.org/10.1088/1361-6455/aa5a88)
- Martin, W. C., & Zalubas, R. 1983, Journal of Physical and Chemical Reference Data, 12, 323, doi: [10.1063/1.555685](https://doi.org/10.1063/1.555685)
- Mc Leod, A. F., Weilbacher, P. M., Ginsburg, A., et al. 2015, ArXiv e-prints. <https://arxiv.org/abs/1511.01914>
- Megeath, S. T., Gutermuth, R., Muzerolle, J., et al. 2012, AJ, 144, 192, doi: [10.1088/0004-6256/144/6/192](https://doi.org/10.1088/0004-6256/144/6/192)

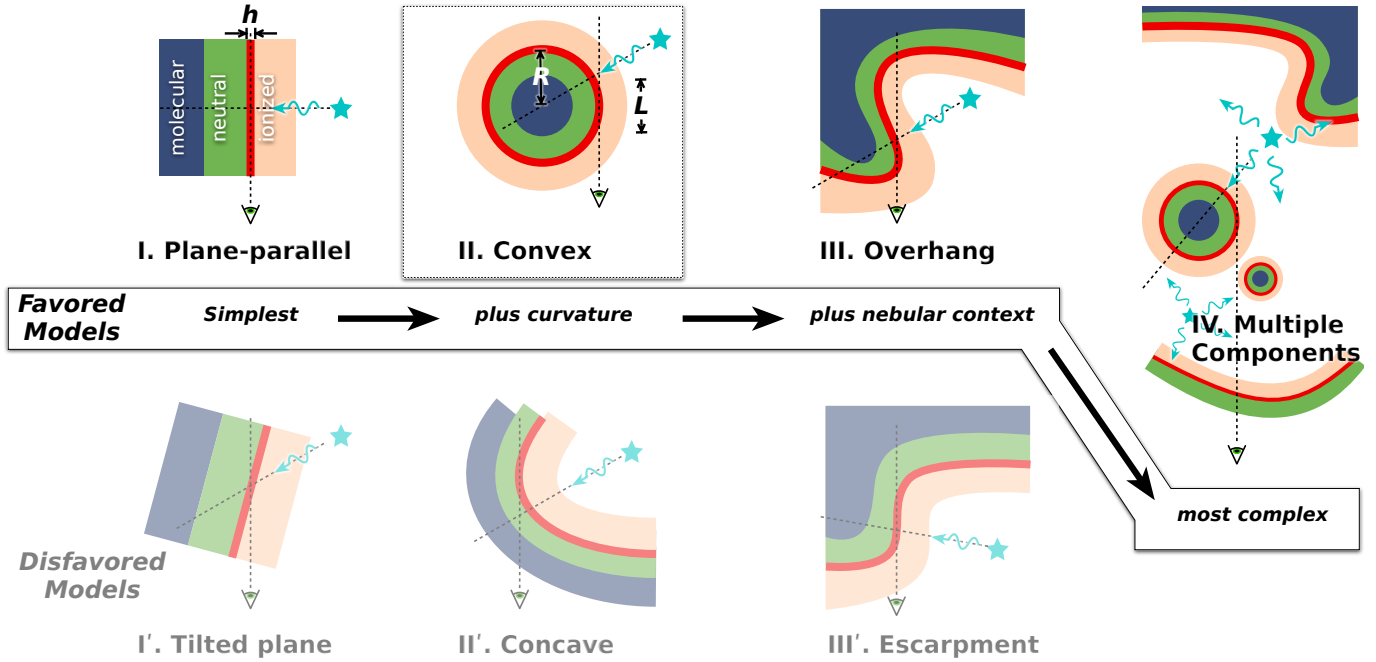


**Figure 10.** Different classes of geometrical models that have been proposed for the Orion Bar. The sequence of models I, II, III, IV are of increasing complexity, but also increasing scope and explanatory power. Models I', II', III', on the other hand, are disfavored due to either underperformance or falsification (see text for further details). For all models, dark blue shading represents molecular gas, green shading represents neutral gas, and light orange shading represents ionized gas. An example emission layer of thickness  $h$  and radius of curvature  $R$  is indicated by thick red lines. The line-of-sight depth of the emission layer is denoted by  $L$ . The direction of illumination and the line of sight are indicated by thin dotted lines.

Moehler, S., Modigliani, A., Freudling, W., et al. 2014, *A&A*, 568, A9, doi: [10.1051/0004-6361/201423790](https://doi.org/10.1051/0004-6361/201423790)

Mohr, P. J., Taylor, B. N., & Newell, D. B. 2008, *Rev. Mod. Phys.*, 80, 633, doi: [10.1103/RevModPhys.80.633](https://doi.org/10.1103/RevModPhys.80.633)

Noll, S., Kausch, W., Barden, M., et al. 2012, *A&A*, 543, A92, doi: [10.1051/0004-6361/201219040](https://doi.org/10.1051/0004-6361/201219040)

Noll, S., Kausch, W., Kimeswenger, S., et al. 2014, *A&A*, 567, A25, doi: [10.1051/0004-6361/201423908](https://doi.org/10.1051/0004-6361/201423908)

Nussbaumer, H., Schmid, H. M., & Vogel, M. 1989, *A&A*, 211, L27

O'Dell, C. R., Ferland, G. J., & Peimbert, M. 2017, *MNRAS*, 464, 4835, doi: [10.1093/mnras/stw2713](https://doi.org/10.1093/mnras/stw2713)

O'Dell, C. R., & Yusef-Zadeh, F. 2000, *AJ*, 120, 382, doi: [10.1086/301429](https://doi.org/10.1086/301429)

Osterbrock, D. E., & Ferland, G. J. 2006, *Astrophysics of gaseous nebulae and active galactic nuclei*, 2nd edn. (Sausalito, CA: University Science Books)

Osterbrock, D. E., Fulbright, J. P., Martel, A. R., et al. 1996, *PASP*, 108, 277, doi: [10.1086/133722](https://doi.org/10.1086/133722)

Parikka, A., Habart, E., Bernard-Salas, J., Köhler, M., & Abergel, A. 2018, *A&A*, 617, A77, doi: [10.1051/0004-6361/201731975](https://doi.org/10.1051/0004-6361/201731975)

Salgado, F., Berné, O., Adams, J. D., et al. 2016, *ApJ*, 830, 118, doi: [10.3847/0004-637X/830/2/118](https://doi.org/10.3847/0004-637X/830/2/118)

Schmid, H. M. 1989, *A&A*, 211, L31

Simón-Díaz, S., Herrero, A., Esteban, C., & Najarro, F. 2006, *A&A*, 448, 351, doi: [10.1051/0004-6361:20053066](https://doi.org/10.1051/0004-6361:20053066)

Smette, A., Sana, H., Noll, S., et al. 2015, *A&A*, 576, A77, doi: [10.1051/0004-6361/201423932](https://doi.org/10.1051/0004-6361/201423932)

Stoerzer, H., & Hollenbach, D. 1998, *ApJ*, 495, 853, doi: [10.1086/305315](https://doi.org/10.1086/305315)

Stoerzer, H., Stutzki, J., & Sternberg, A. 1997, *A&A*, 323, L13

Subrahmanyam, R., Goss, W. M., & Malin, D. F. 2001, *AJ*, 121, 399, doi: [10.1086/318017](https://doi.org/10.1086/318017)

van der Werf, P. P., Goss, W. M., & O'Dell, C. R. 2013, *ApJ*, 762, 101, doi: [10.1088/0004-637X/762/2/101](https://doi.org/10.1088/0004-637X/762/2/101)

van der Werf, P. P., Stutzki, J., Sternberg, A., & Krabbe, A. 1996, *A&A*, 313, 633

Van Hoof, P. A. M. 2018, *Galaxies*, 6, doi: [10.3390/galaxies6020063](https://doi.org/10.3390/galaxies6020063)

Walmsley, C. M., Natta, A., Oliva, E., & Testi, L. 2000, *A&A*, 364, 301

Watson, A. M., Henney, W. J., & Escalante, V. 1998, in *American Astronomical Society Meeting Abstracts*, Vol. 193, 16.03

Weilbacher, P. M., Monreal-Ibero, A., Kollatschny, W., et al. 2015, *A&A*, 582, A114, doi: [10.1051/0004-6361/201526529](https://doi.org/10.1051/0004-6361/201526529)

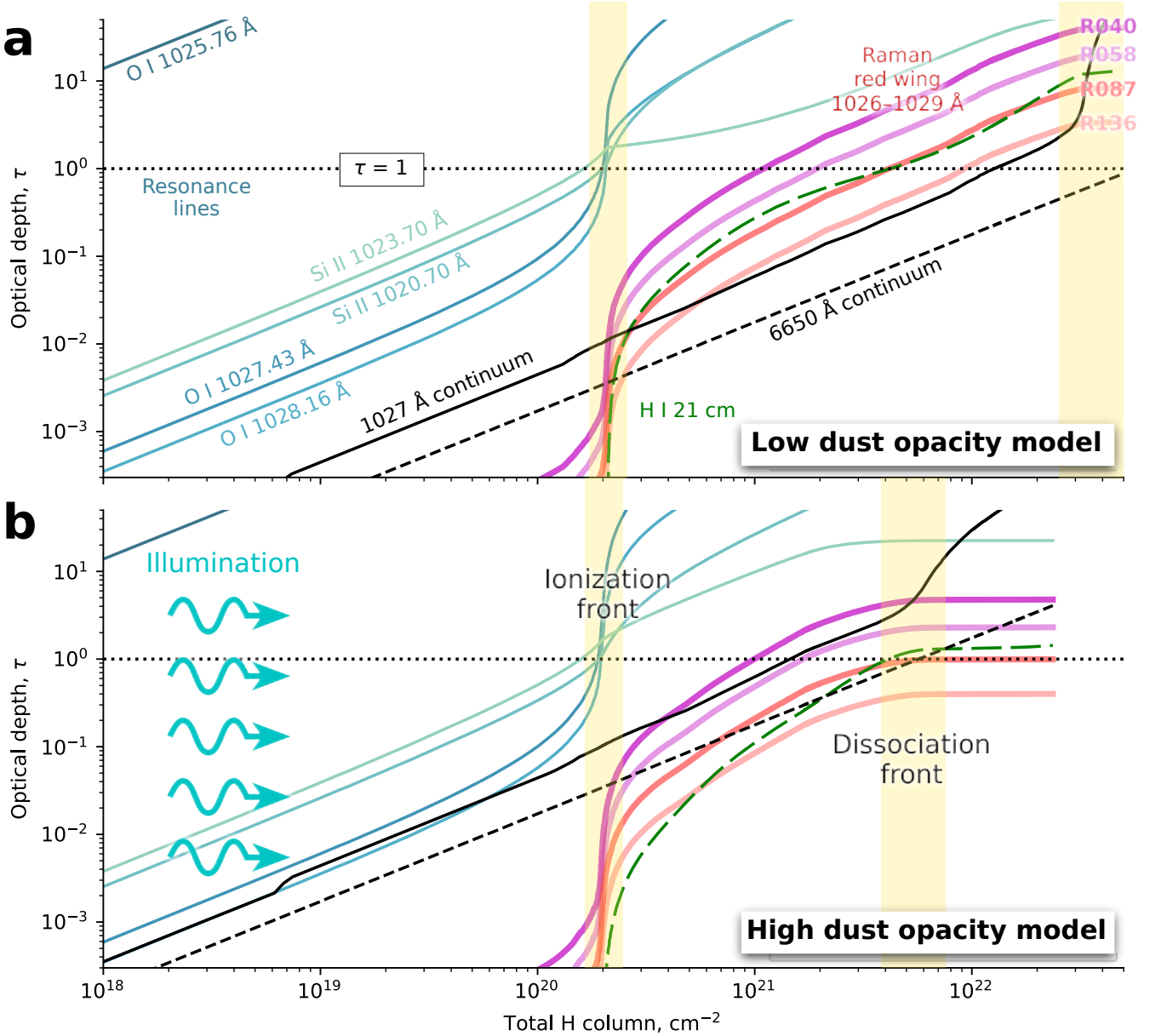


**Figure 11.** Optical depth of select processes as a function of total hydrogen nucleon column density, calculated from static Cloudy simulations of the Orion Bar. All optical depths and columns are measured with respect to the illuminating Trapezium stars, which are situated to the left in this figure. Separate panels show two models that differ only in the assumed dust absorption opacity: (a) low opacity,  $\sigma_{\text{FUV}} \approx 5 \times 10^{-23} \text{ cm}^2 \text{ H}^{-1}$ , and (b) high opacity,  $\sigma_{\text{FUV}} \approx 5 \times 10^{-22} \text{ cm}^2 \text{ H}^{-1}$ . Optical depths of  $\text{O}^0$  and  $\text{Si}^+$  absorption lines in the Ly $\beta$  wings are shown in blue. Continuum optical depths near Ly $\beta$  (solid line) and H $\alpha$  (dashed line) are shown in black. The H $^0$  21 cm line optical depth is shown in green (long dashed line). Optical depths to Rayleigh/Raman scattering for 4 observed bands in the red wing of Ly $\beta$  (see Table 2) are shown in red.

## APPENDIX

### A. REANALYSIS OF 21 CM H<sub>I</sub> OBSERVATIONS OF THE ORION BAR

Karl G. Jansky Very Large Array observations of the H<sub>I</sub> 21 cm line from the Orion Nebula and its surroundings at a spatial resolution of  $\approx 6''$  and a velocity resolution of  $0.77 \text{ km s}^{-1}$  were presented in van der Werf et al. (2013, hereafter vdW13). The line is seen both in emission and absorption of the strong free-free continuum emitted by the ionized nebula. The majority of

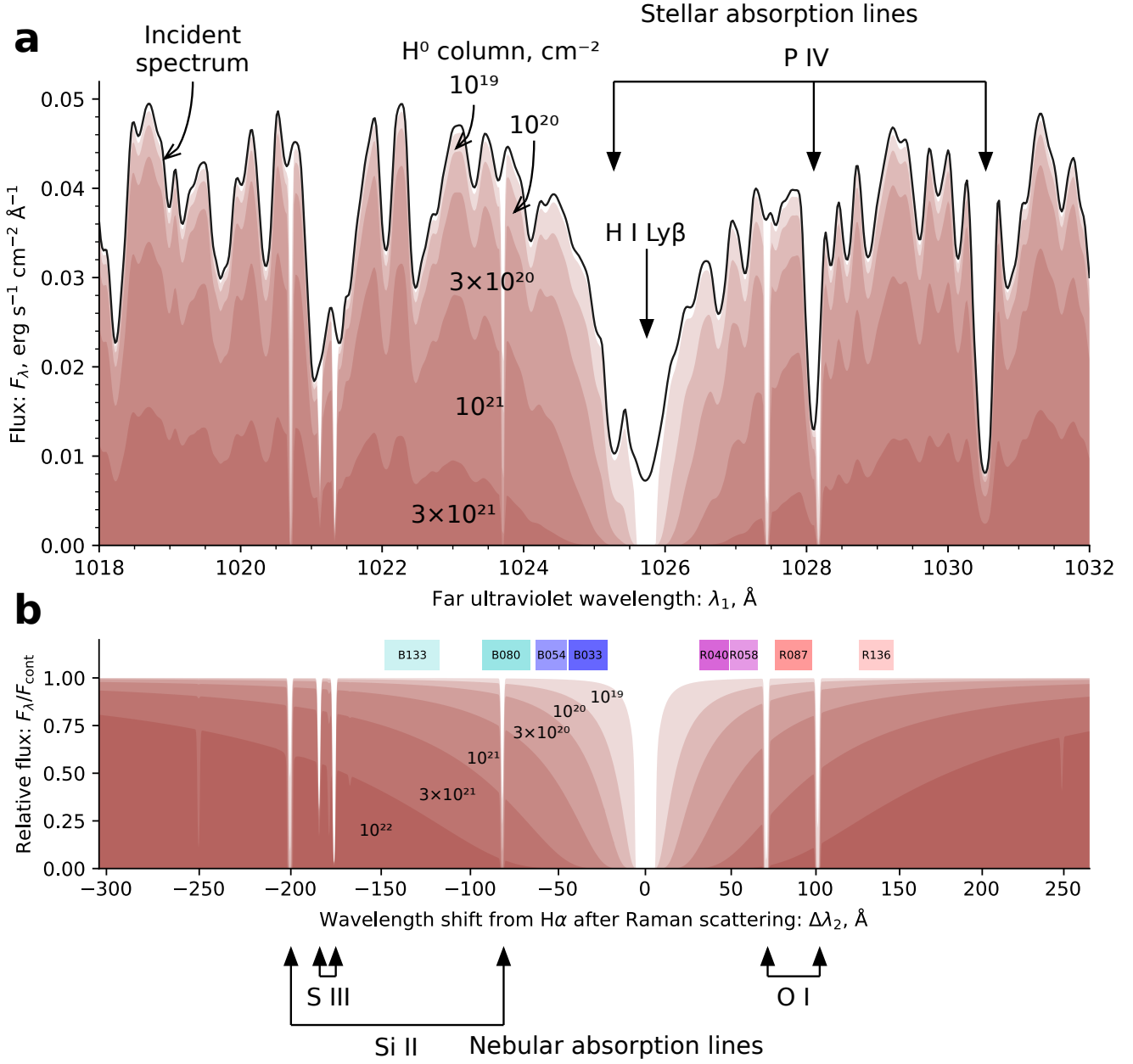


**Figure 12.** (a) Predicted spectrum of Trapezium stars in vicinity of Ly $\beta$  from POWR OB atmosphere models (black line), together with attenuation by Cloudy model of the Orion Bar (red filled shapes), extracted at a series of values of the neutral hydrogen column density, as marked. (b) Relative attenuation of the incident spectrum by line opacity only (that is, neglecting dust continuum opacity) in the Cloudy models, which shows the development of the Ly $\beta$  damping wings as the column density increases. In this panel, the  $x$  axis is labelled with  $\Delta\lambda_2$  in the optical domain, allowing direct comparison with the observations presented in Figure 9 (observed Raman bands are indicated by colored boxes). Note that the scale is linear in  $\lambda_1$ , which is slightly non-linear in  $\Delta\lambda_2$ . Wavelengths of some of the more prominent stellar photospheric lines and nebular absorption lines are marked.

the absorption arises in the foreground Veil at Local Standard of Rest velocities of  $v_{\text{lsr}} = -2 \text{ km s}^{-1}$  to  $+7 \text{ km s}^{-1}$ . Emission is seen primarily at more redshifted velocities of  $+10 \text{ km s}^{-1}$  to  $+15 \text{ km s}^{-1}$ , similar to the velocities of the molecular gas seen in CO, although at large distances from the center of the nebula the Veil is also seen in emission. The analysis of the absorption components by vdW13 was carried out under the assumptions that (i) all of the continuum emission arises from *behind* the absorbing H<sup>0</sup> column (from the point of view of the Earth), and (ii) line emission is negligible at velocities where absorption is

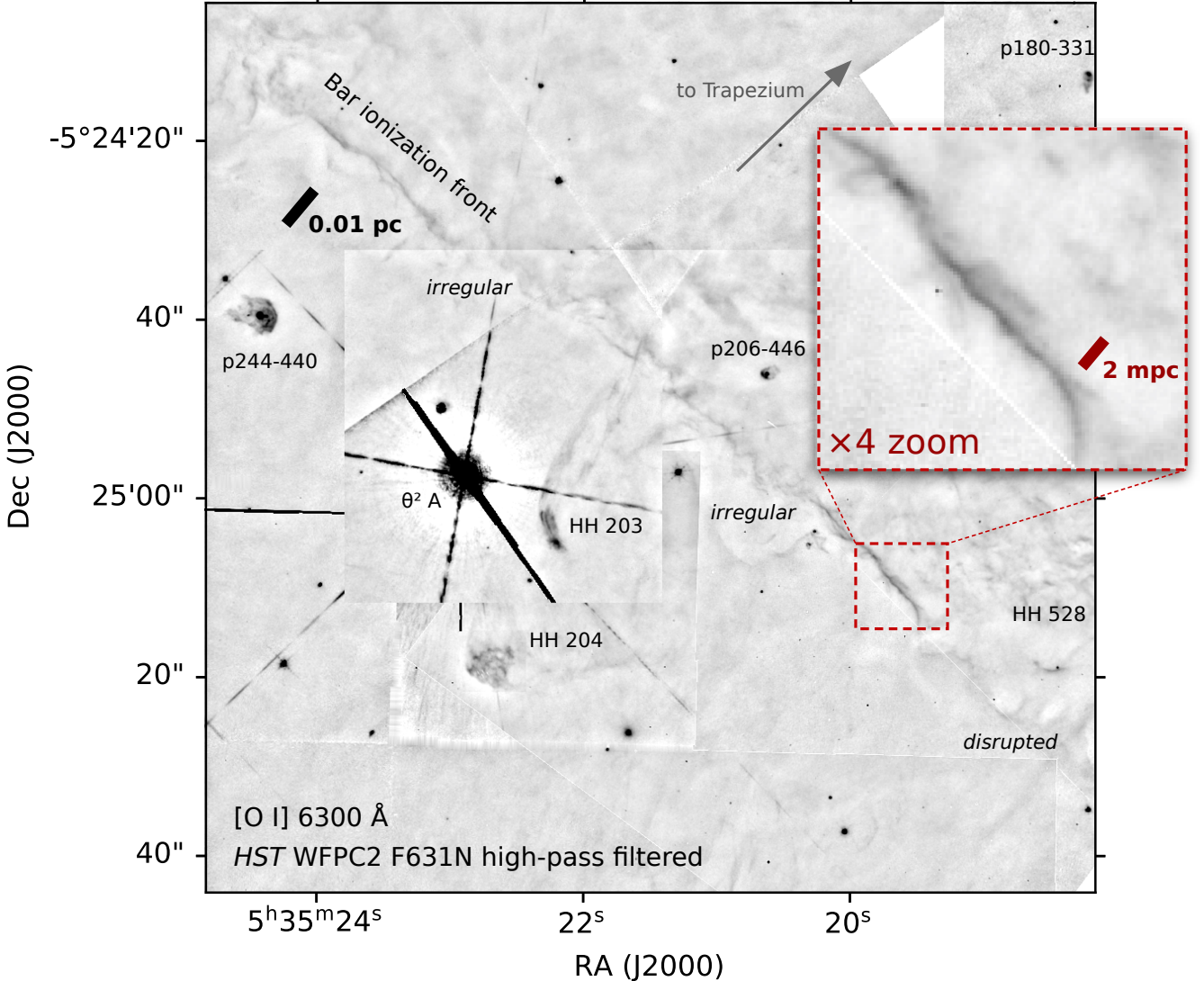


**Figure 13.** Fine-scale structure of the ionization front at the Orion Bar.

detected. These are both very good assumptions in the case of absorption by the foreground Veil, but they break down for the case of the Orion Bar, where both emission and absorption are seen at similar velocities and in spatially adjacent regions. Given the wealth of information on the physical conditions and geometry that these data provide, it is worth reanalyzing them under less restrictive assumptions.

In the Rayleigh-Jeans limit, the frequency-dependent surface brightness  $I_\nu$  is characterized by the brightness temperature in each velocity channel:  $T_b(v) = c^2 I_\nu / 2k\nu^2$ , where  $v/c = (\nu/\nu_0) - 1$  and  $\nu_0 = 1.420\,405$  GHz. The radiative transfer equation can be solved for an idealized three-layer sandwich structure (see Fig. 15), consisting of (1) a background  $H^+$  region with electron temperature  $T_e$  and free-free continuum optical depth  $\tau'$ , (2) an intermediate neutral  $H^0$  layer with spin temperature  $T_s$  and line optical depth  $\tau(v)$ , and (3) a foreground  $H^+$  region with the electron temperature  $T_e$  and free-free continuum optical depth  $\tau''$ . The continuum source function in regions 1 and 3 is  $T_e$ , whereas the line source function in region 2 is  $T_s$ . Region 2 is assumed to have zero continuum optical depth. Following vdW13, large-scale Milky Way  $H\alpha$  line emission along the line of sight through Orion is neglected since it is (a) very faint compared with the nebula, with  $T_b(v) < 48$  K at  $v = 10\text{ km s}^{-1}$  (Green 1991; Green & Padman 1993), and (b) any emission that is smooth on angular scales below 7 arcminutes will be filtered out by the interferometer.

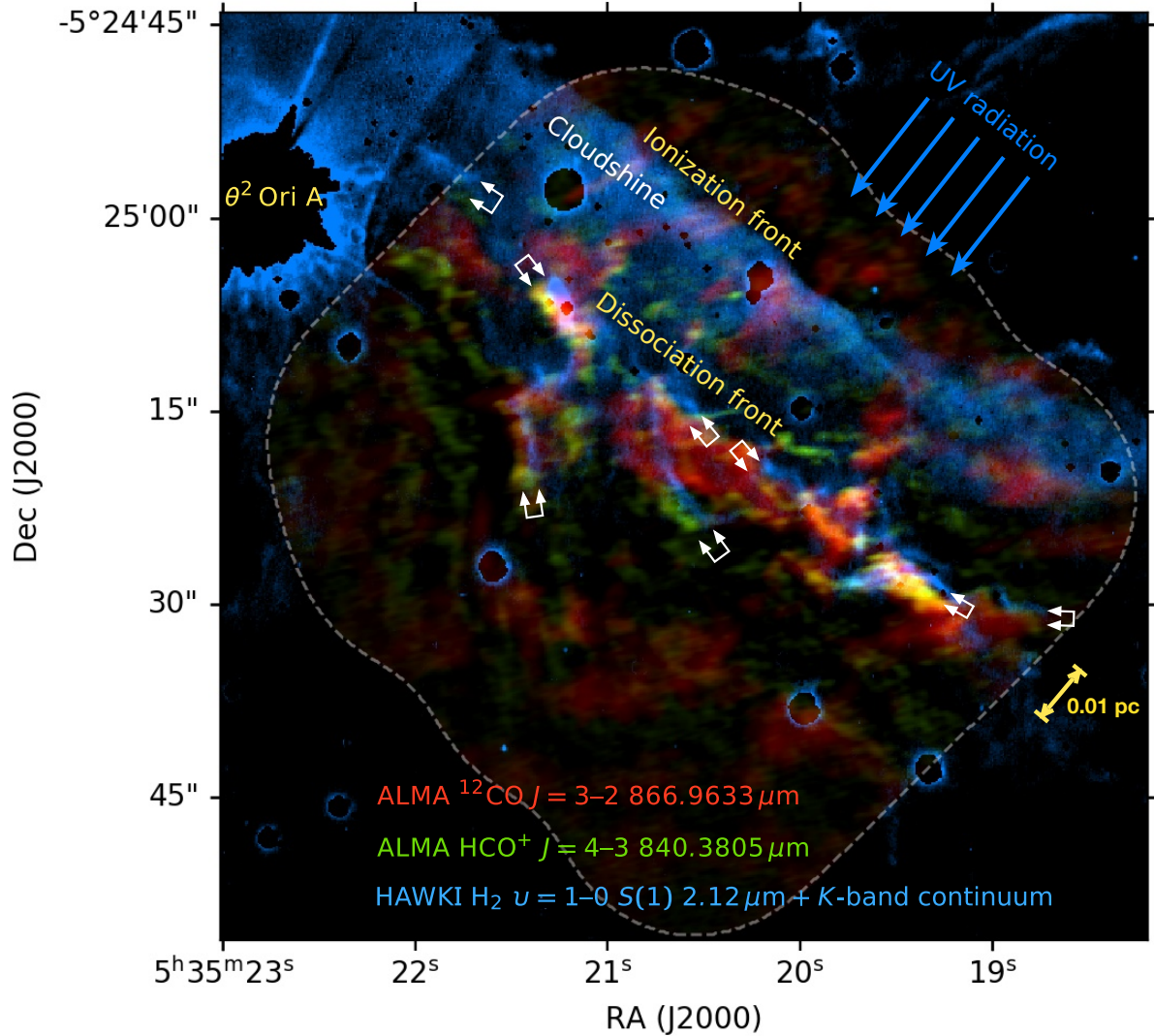


**Figure 14.** Fine-scale structure of the dissociation front in the Orion Bar. Double white arrows mark out some instances of stratification between emission of H<sub>2</sub> (blue) and heavier molecules (green/yellow/red). In every instance H<sub>2</sub> is displaced towards the irradiated side of the filament by 1" to 2" ( $\approx 0.003$  pc). Background image shows ALMA mosaics (Goicoechea et al. 2016) of the sub-mm CO  $J = 3 \rightarrow 2$  866.96  $\mu\text{m}$  HCO<sup>+</sup> 840.38  $\mu\text{m}$  emission lines in the red and green color channels, respectively, with the boundary of the ALMA field shown by the gray dashed line. The blue color channel of the background image shows near-infrared vibrationally excited H<sub>2</sub>  $v = 1 \rightarrow 0$   $S(1)$  2.12  $\mu\text{m}$  emission, extracted from narrow-band imaging with ESO's High Acuity Wide-field Imager (HAWK-I, Kissler-Patig et al. 2008). The H<sub>2</sub> image has been corrected for contamination by ionized emission (mainly hydrogen Brγ recombination line), but has not been continuum-subtracted. As a result, scattered starlight (cloudshine, Foster & Goodman 2006) is seen as a band of diffuse emission that falls off smoothly behind the ionization front.

**Figure 15.** Three-layer sandwich structure for H I 21 cm radiative transfer.

At continuum frequencies just off the line,  $\tau(v) = 0$  and only regions 1 and 3 contribute to the observed brightness, yielding a continuum brightness temperature

$$\begin{aligned} T_c &= T_e \left( 1 - e^{-(\tau' + \tau'')} \right) \\ &= T_c' e^{-\tau''} + T_c'', \end{aligned} \tag{A1}$$

where the second equality gives the decomposition into separate contributions from region 1:  $T_c' = T_e(1 - e^{-\tau'})$ , and region 3:  $T_c'' = T_e(1 - e^{-\tau''})$ . At frequencies where the line opacity is significant, all three regions contribute, yielding

$$T_b(v) = T_c' e^{-(\tau(v)+\tau'')} + T_s \left(1 - e^{-\tau(v)}\right) e^{-\tau''} + T_c''. \quad (\text{A2})$$

For practical reasons related to the deconvolution of the interferometric data, the results of vdW13 are presented in continuum-free form as  $\tilde{T}_b(v) = T_b(v) - T_c$ . Combining equation (A1) and (A2), one finds

$$\tilde{T}_b(v) = [1 - e^{-\tau(v)}] [1 - (T_c''/T_e)] [T_s - T_c']. \quad (\text{A3})$$

The relative brightness temperature of the line,  $\tilde{T}_b(v)$ , is therefore seen to be the product of three factors, given by the three sets of square brackets in equation (A3). The first two factors are always positive since  $\tau(v) \geq 0$  and  $T_c'' \leq T_e$ , but the third factor can take either sign. When the continuum brightness temperature  $T_c'$  of the background photoionized gas in region 1 exceeds the spin temperature  $T_s$  of neutral hydrogen in region 2, then we see an absorption line:  $\tilde{T}_b(v) < 0$ . On the other hand, when  $T_s$  is higher than  $T_c'$ , then we see an emission line:  $\tilde{T}_b(v) > 0$ . In either case, the maximum line strength will be found when region 2 is opaque ( $\tau(v) \gg 1$ ) and region 3 is transparent ( $T_c'' \ll T_e$ ), yielding  $\max(|\tilde{T}_b(v)|) = |T_s - T_c'|$ .

The electron temperature in the ionized gas is expected to be roughly constant at  $T_e \approx 11\,000$  K (Dicker et al. 2009), but this still leaves 4 unknown quantities,  $\tau(v)$ ,  $T_s$ ,  $T_c'$ , and  $T_c''$ , to be determined from 2 observed quantities:  $T_c$  and  $\tilde{T}_b(v)$ . Further assumptions must therefore be made in order to interpret the observations, but these can be guided by the observed spatial trends and simple geometric models. For instance, in the Orion Bar the free-free continuum brightness temperature falls sharply across the ionization front from  $T_c \approx 3000$  K on the ionized side, but then levels off to a roughly constant value of  $T_c \approx 600$  K on the neutral side. Assuming that this constant value reflects unrelated foreground emission (probably ionized by  $\theta^2$  Ori A) that overlays the entire Bar (this hypothesis is tested below), we have an upper limit to the background emission of  $T_c - 600$  K. It can be further assumed that the emission from region 1 is a constant fraction,  $f_{\text{bg}}$ , of this upper limit:

$$T_c' = f_{\text{bg}}(T_c - 600 \text{ K}). \quad (\text{A4})$$

If the Bar geometry is a cylinder that is illuminated from the side (see Fig. XXX), then  $f_{\text{bg}} = 0.5$  is appropriate. If the Bar is illuminated from slightly behind, or if it is an escarpment, or if an additional background component is present (see § 5.1), then the fraction will be larger:  $0.5 < f_{\text{bg}} < 1.0$ .

Further progress can then be made by considering null points in the nebula where line emission and absorption cancel out. At such points  $\tilde{T}_b(v) \approx 0$ , so that  $T_s = T_c'$  by equation (A3). Absorption component M is identified by vdW13 as associated with H<sup>0</sup> in the Bar, due to its velocity and spatial distribution. Component M consists of a string of knots with  $\tilde{T}_b(v) = -200$  to  $-400$  K at  $v \approx 11 \text{ km s}^{-1}$ . They are arranged parallel to the Bar, just behind the ionization front at a relative position of roughly  $+0.006$  pc (see Fig. 5) and where the continuum brightness has fallen to  $T_c \approx 2200$  K. At greater distances from the ionization front the H<sub>I</sub> at this velocity is seen in emission, reaching a peak of  $\tilde{T}_b(v) \approx +250$  K at  $+0.030$  pc where  $T_c \approx 750$  K. The crossover null point where  $\tilde{T}_b(v) = 0$  occurs between these two at  $+0.012$  pc where  $T_c \approx 1500$  K.

*Add a table showing*